Emergent pseudospin-1 Maxwell fermions with a threefold degeneracy in optical lattices

Yan-Qing Zhu,[1] Dan-Wei Zhang,[2,*] Hui Yan,[2] Ding-Yu Xing,[1,3] and Shi-Liang Zhu[1,2,4,†]

[1]*National Laboratory of Solid State Microstructures and School of Physics, Nanjing University, Nanjing 210093, China*
[2]*Guangdong Provincial Key Laboratory of Quantum Engineering and Quantum Materials, SPTE,*
South China Normal University, Guangzhou 510006, China
[3]*Collaborative Innovation Center of Advanced Microstructures, Nanjing 210093, China*
[4]*Synergetic Innovation Center of Quantum Information and Quantum Physics, University of Science and Technology of China,*
Hefei, Anhui 230026, China

The discovery of relativistic spin-1/2 fermions such as Dirac and Weyl fermions in condensed-matter or artificial systems opens a new era in modern physics. An interesting but rarely explored question is whether other relativistic spinal excitations could be realized with artificial systems. Here, we construct two- and three-dimensional tight-binding models realizable with cold fermionic atoms in optical lattices, where the low energy excitations are effectively described by the spin-1 Maxwell equations in the Hamiltonian form. These relativistic (linear dispersion) excitations with unconventional integer pseudospin, beyond the Dirac-Weyl-Majorana fermions, are an exotic kind of fermions named as Maxwell fermions. We demonstrate that the systems have rich topological features. For instance, the threefold degenerate points called Maxwell points may have quantized Berry phases and anomalous quantum Hall effects with spin-momentum locking may appear in topological Maxwell insulators in the two-dimensional lattices. In three dimensions, Maxwell points may have nontrivial monopole charges of ± 2 with two Fermi arcs connecting them, and the merging of the Maxwell points leads to topological phase transitions. Finally, we propose realistic schemes for realizing the model Hamiltonians and detecting the topological properties of the emergent Maxwell quasiparticles in optical lattices.

I. INTRODUCTION

Discovery of new particles in nature or new quasiparticles in condensed-matter systems is at the heart of modern physics [1]. One of the remarkable examples is the discovery of relativistic Dirac fermions emerged from graphene, which has attracted great interest in physics [2]. Furthermore, it was demonstrated that Weyl fermions, which are massless spin-1/2 particles according to quantum field theory and never before observed as fundamental particles in nature, can emerge as quasiparticles in condensed matter [3–9] or photonic crystals [10,11]. Most interestingly, Dirac and Weyl fermions have rich topological features [2–13]. However, quasiparticles with higher spin numbers are also fundamentally important but rarely studied in condensed-matter physics or artificial systems [14–16]. Recently, a pioneer work in this direction theoretically predicted that "new fermions" (fermionic quasiparticle excitations) beyond the Dirac-Weyl-Majorana classification can emerge in some band structures with three- or morefold degenerate points in the presence of time-reversal symmetry [14]. Very recently, the observation of three-component new fermions in the topological semimetal molybdenum phosphide has been reported [17]. Although it may be difficult to find these (and other) new fermions in condensed-matter systems, they may also emerge from well-designed and tunable ultracold atomic systems, especially since Dirac and Weyl fermions have already been well studied in the field of cold atoms [18–24].

In this paper, we propose and analyze an exotic kind of pseoduspin-1 fermions in two-dimensional (2D) square and three-dimensional (3D) cubic optical lattices, dubbed "Maxwell fermions" as they are analogous to massless spin-1 photons described by the Maxwell equations. We first rewrite the Maxwell equations in an anisotropic medium in the form of the Schrödinger equation and then construct 2D and 3D tight-binding models, where the low-energy excitations are described by the Maxwell Hamiltonian. With a tunable parameter, the systems can be varied in different quantum phases: topological or normal Maxwell insulator, and topological or normal Maxwell metal. The topological Maxwell metal is characterized by threefold degenerate points, known as Maxwell points, which have nontrivial monopole charges or quantized Berry phases and the low-energy excitation near the Maxwell point behaved like a photon described by the Maxwell equations. In the 2D system, we find interesting spin-momentum locking edge states in the Maxwell insulating phase, which is in analogy with the circularly polarized polarization of the photons. In the 3D system, the topological properties of Maxwell fermions are similar to those of the Weyl fermions in Weyl semimetals, and the Maxwell points have monopole charges of ± 2 with two Fermi arcs connecting them. The experimental scheme for implementation (and detection) of our models using three-component ultracold atoms in optical lattices is presented. Although some threefold band degeneracies were revealed in solid-state systems with the body-centered lattice structure and time-reversal symmetry in Ref. [14], our proposal is essentially different. First, our threefold Maxwell points in 3D exist when the time-reversal symmetry of the system is broken, in which case the threefold band degeneracies in Ref. [14] will split into a number of Weyl points. Thanks to the broken time-reversal symmetry, the

minimal number of threefold degeneracies in our 3D system can be two (which is thus a minimal model), instead of four in Ref. [14]. In addition, we use three atomic internal states to form the pseudospin-1 basis and thus only the simple cubic lattice is used in our proposal, in contrast to the required body-centered cubic lattices for spin-1/2 electrons in real materials. This enables us to realize exotic threefold fermions in a lattice of simplest geometry.

The paper is organized as follows. In Sec. II, we rewrite the Maxwell equations in the Schrödinger form and then present the general idea of realizing Maxwell fermionic quasiparticles in lattice systems. Section III introduces the 2D square-lattice model for realizing the Maxwell metals and insulators, and explores the topological properties of the emergent Maxwell fermions. In Sec. IV, we proceed to study the properties of 3D Maxwell fermions in the cubic-lattice model. In Sec. V, we propose schemes for realization of the model Hamiltonian and detection of the topological Chern numbers in the optical lattices. Finally, a brief discussion and a short conclusion are given in Sec. VI.

II. MAXWELL HAMILTONIAN AND MAXWELL FERMIONS IN LATTICE SYSTEMS

In this section, we first rewrite the Maxwell equations in an anisotropic medium in the form of the Schrödinger's equation, and then describe the general scheme for realizing the Maxwell fermions in artificial lattice systems.

A. Maxwell equations in Schrödinger's form

In a region absent of charges and currents, the well-known Maxwell equations in matter are given by

$$\nabla \times \mathbf{E} = -\frac{\partial \mathbf{B}}{\partial t}, \quad \nabla \cdot \mathbf{E} = 0,$$

$$\nabla \times \mathbf{H} = \frac{\partial \mathbf{D}}{\partial t}, \quad \nabla \cdot \mathbf{B} = 0, \quad (1)$$

where the displacement field $\mathbf{D} = \varepsilon_0 \varepsilon_r \mathbf{E}$, with $\mathbf{E}$ being the electric field, and the magnetic field $\mathbf{B} = \mu_0 \mu_r \mathbf{H}$, with $\mathbf{H}$ being the magnetizing field. Here ε_0 (μ_r) is the permittivity (permeability) of free space, and ε_r and μ_r are the relative permittivity and permeability, respectively. In an anisotropic medium, ε_r and μ_r are tensors rather than numbers. To simplify the proceeding analysis, we assume that the tensors ε_r and μ_r are simultaneously diagonalized, then the relationships between $\mathbf{D}$ and $\mathbf{E}$, $\mathbf{B}$ and $\mathbf{H}$ now become

$$\begin{pmatrix} D_x \\ D_y \\ D_z \end{pmatrix} = \varepsilon_0 \begin{pmatrix} \varepsilon_x & 0 & 0 \\ 0 & \varepsilon_y & 0 \\ 0 & 0 & \varepsilon_z \end{pmatrix} \begin{pmatrix} E_x \\ E_y \\ E_z \end{pmatrix},$$

$$\begin{pmatrix} B_x \\ B_y \\ B_z \end{pmatrix} = \mu_0 \begin{pmatrix} \mu_x & 0 & 0 \\ 0 & \mu_y & 0 \\ 0 & 0 & \mu_z \end{pmatrix} \begin{pmatrix} H_x \\ H_y \\ H_z \end{pmatrix}. \quad (2)$$

Thus Eq. (1) can be rewritten as

$$\epsilon_{\alpha\beta\gamma} \frac{\partial E_\gamma}{\partial \beta} = -\frac{\partial B_\alpha}{\partial t} \Rightarrow \frac{c}{\sqrt{\varepsilon_\gamma \mu_\alpha}} \epsilon_{\alpha\beta\gamma} \frac{\partial \tilde{E}_\gamma}{\partial \beta} = -\frac{\partial \tilde{H}_\alpha}{\partial t},$$

$$\epsilon_{\alpha\beta\gamma} \frac{\partial H_\gamma}{\partial \beta} = \frac{\partial D_\alpha}{\partial t} \Rightarrow \frac{c}{\sqrt{\varepsilon_\alpha \mu_\gamma}} \epsilon_{\alpha\beta\gamma} \frac{\partial \tilde{H}_\gamma}{\partial \beta} = \frac{\partial \tilde{E}_\alpha}{\partial t}, \quad (3)$$

where $\tilde{E}_\alpha = \sqrt{\varepsilon_0 \varepsilon_\alpha} E_\alpha$, $\tilde{H}_\alpha = \sqrt{\mu_0 \mu_\alpha} H_\alpha$, and $c = 1/\sqrt{\varepsilon_0 \mu_0}$. Then we define the photon wave function as [25,26]

$$\mathbf{\Phi}(\mathbf{r}, t) = \tilde{\mathbf{E}}(\mathbf{r}, t) + i \tilde{\mathbf{H}}(\mathbf{r}, t),$$

we have $\nabla \cdot \mathbf{\Phi} = 0$, and

$$i\hbar \frac{\partial \Phi_m^\alpha}{\partial t} = v_{\alpha\gamma} (i\epsilon_{\alpha\beta\gamma}) \frac{\hbar}{i} \frac{\partial \tilde{E}_\gamma}{\partial \beta} + i v_{\gamma\alpha} (i\epsilon_{\alpha\beta\gamma}) \frac{\hbar}{i} \frac{\partial \tilde{H}_\gamma}{\partial \beta}, \quad (4)$$

where $v_{\alpha\gamma} = c/\sqrt{\varepsilon_\alpha \mu_\gamma}$, $v_{\gamma\alpha} = c/\sqrt{\varepsilon_\gamma \mu_\alpha}$, and $\hat{P}_\beta = -i\hbar\partial_\beta$. When $\varepsilon_\alpha \mu_\gamma = \varepsilon_\gamma \mu_\alpha$, that is, $v_{\alpha\gamma} = v_{\gamma\alpha}$ [the condition for obtaining a Hermitian Hamiltonian, see Eq. (6)], then we can further rewrite Eq. (4) as

$$i\hbar \frac{\partial \Phi_m^\alpha}{\partial t} = v_{\alpha\gamma} (i\epsilon_{\alpha\beta\gamma}) \hat{P}_\beta \Phi_m^\gamma. \quad (5)$$

We hence obtain the following Schrödinger's equation:

$$i\hbar \frac{\partial}{\partial t} \begin{pmatrix} \Phi_m^x \\ \Phi_m^y \\ \Phi_m^z \end{pmatrix} = \begin{pmatrix} 0 & -iv_{xy}\hat{P}_z & iv_{xz}\hat{P}_y \\ iv_{yx}\hat{P}_z & 0 & -iv_{yz}\hat{P}_x \\ -iv_{zx}\hat{P}_y & iv_{zy}\hat{P}_x & 0 \end{pmatrix} \begin{pmatrix} \Phi_m^x \\ \Phi_m^y \\ \Phi_m^z \end{pmatrix}. \quad (6)$$

This corresponds to the Maxwell equations in the anisotropic medium in the Schrödinger's form

$$i\hbar \frac{\partial}{\partial t} \mathbf{\Phi} = \hat{H}_M \mathbf{\Phi}, \quad (7)$$

where the Hamiltonian is given by

$$\hat{H}_M = v_x \hat{S}_x \hat{P}_x + v_y \hat{S}_y \hat{P}_y + v_z \hat{S}_z \hat{P}_z. \quad (8)$$

Here $\hat{S}_\beta = (\hat{S}_{\alpha\gamma})^\beta = i\epsilon_{\alpha\beta\gamma}$ and $\epsilon_{\alpha\beta\gamma}$ ($\alpha, \beta, \gamma = x, y, z$) is the Levi-Civita symbol. Noted that, $v_x = v_{yz} = v_{zy}$, $v_y = v_{zx} = v_{xz}$, and $v_z = v_{xy} = v_{yx}$ are the necessary and sufficient condition to obtain a Hermitian Hamiltonian in Eq. (6). A typical case when $\varepsilon_r = \mu_r = 1$, it returns to the free-space situation and we obtain the related Hamiltonian of single photon in vacuum as $\hat{H}_M = c\hat{\mathbf{S}} \cdot \hat{\mathbf{P}}$. Here $\hat{\mathbf{S}} = (\hat{S}_x, \hat{S}_y, \hat{S}_z)$ are the spin matrices for a particle of spin-1, which are defined as

$$\hat{S}_x = \hat{S}^1 = i \begin{pmatrix} \varepsilon_{111} & \varepsilon_{112} & \varepsilon_{113} \\ \varepsilon_{211} & \varepsilon_{212} & \varepsilon_{213} \\ \varepsilon_{311} & \varepsilon_{312} & \varepsilon_{313} \end{pmatrix} = \begin{pmatrix} 0 & 0 & 0 \\ 0 & 0 & -i \\ 0 & i & 0 \end{pmatrix},$$

$$\hat{S}_y = \hat{S}^2 = i \begin{pmatrix} \varepsilon_{121} & \varepsilon_{122} & \varepsilon_{123} \\ \varepsilon_{221} & \varepsilon_{222} & \varepsilon_{223} \\ \varepsilon_{321} & \varepsilon_{322} & \varepsilon_{323} \end{pmatrix} = \begin{pmatrix} 0 & 0 & i \\ 0 & 0 & 0 \\ -i & 0 & 0 \end{pmatrix},$$

$$\hat{S}_z = \hat{S}^3 = i \begin{pmatrix} \varepsilon_{131} & \varepsilon_{132} & \varepsilon_{133} \\ \varepsilon_{231} & \varepsilon_{232} & \varepsilon_{233} \\ \varepsilon_{331} & \varepsilon_{332} & \varepsilon_{333} \end{pmatrix} = \begin{pmatrix} 0 & -i & 0 \\ i & 0 & 0 \\ 0 & 0 & 0 \end{pmatrix}. \quad (9)$$

One can check that $[\hat{S}_x, \hat{S}_y] = i\hat{S}_z$, $\hat{\mathbf{S}} \times \hat{\mathbf{S}} = i\hat{\mathbf{S}}$, and $\hat{\mathbf{S}}^2 = \hat{S}_x^2 + \hat{S}_y^2 + \hat{S}_z^2 = S(S+1)$ with $S = 1$. These matrices are the three generators of SU(3) group which have eight generators called Gell-Mann matirces. Equation (8) is a relativistic Hamiltonian to discuss a particle with pseudospin-1, which is analogous to the Weyl equation for the massless relativistic fermions with spin-1/2.

B. Maxwell fermions in lattice systems

The Maxwell Hamiltonian in Eq. (8) originally describes a massless relativistic boson (photon) with spin one. Moreover, in quantum field theory, bosons are identical particles with zero or integer spins, while fermions are particles with half integer spins. So it seems that the Maxwell Hamiltonian cannot be used to describe the fermionic particles. However, there is a fundamental difference between particles in a lattice and those at high-energy. Rather than constrained by Poincaré symmetry in high-energy physics, quasiparticles in a lattice system are constrained only by certain subgroups (space groups) of the Poincaré symmetry [14]. So there is the potential to find free fermionic excitations in lattice systems for which the Hamiltonian is written in the form of Eq. (8). In the subsequent sections, we demonstrate that the Bloch Hamiltonian of certain well-designed lattice models can be written as

$$\mathcal{H}(\mathbf{k}) = \mathbf{R}(\mathbf{k}) \cdot \hat{\mathbf{S}}, \qquad (10)$$

where $\mathbf{R}(\mathbf{k}) = (R_x, R_y, R_z)$ denotes the Bloch vectors. Some threefold degenerate points exist in the bands of the model Hamiltonian where low-energy physics should be described by the Schrödinger equation with the Hamiltonian (8), and thus we call such quasiparticles Maxwell quasiparticles. Potential candidates include atoms in the optical lattices, electrons in certain crystals, and photons in photonic lattices. Here we focus on the fermionic atoms in optical lattices. For these fermionic atoms, the Maxwell quasiparticles are fermions instead of bosons (spin-1 photons) in the original Maxwell equations. In principle, Maxwell fermions can be realized with two different schemes. First, we can use noninteracting fermionic atoms in a square or cubic optical lattice and choose three atomic internal states in the ground-state manifold to encode the three spin states $|s\rangle$ ($s = \uparrow, 0, \downarrow$). Notably, the use of the atomic internal degree of freedom enables us to implement our model in a lattice of simplest geometry, i.e., a primitive square or cubic lattice. Alternatively, Maxwell fermions can be realized by using single-component fermionic atoms in optical lattices with three sublattices, where the pseudospin-1 basis is replaced by the three sublattices in a unit cell. For conceptual simplicity, we discuss the first scheme in the main text, and the realization of the second scheme is addressed in Appendix A.

III. MAXWELL FERMIONS IN 2D LATTICE SYSTEMS

In this section, we construct a 2D tight-binding model on a square lattice and then investigate the intrinsic properties of the emergent pseudospin-1 Maxwell fermions in different topological phases.

A. 2D model

The 2D model Hamiltonian we considered is given by

$$\hat{H}_{2D} = t \sum_{\mathbf{r}} [\hat{H}_{\mathbf{rx}} + \hat{H}_{\mathbf{ry}} + (\Gamma_0 \hat{a}_{\mathbf{r},0}^\dagger \hat{a}_{\mathbf{r},\uparrow} + \text{H.c.})],$$

$$\hat{H}_{\mathbf{rx}} = -\hat{a}_{\mathbf{r-x},0}^\dagger (\hat{a}_{\mathbf{r},\downarrow} + i\hat{a}_{\mathbf{r},\uparrow}) + \hat{a}_{\mathbf{r+x},0}^\dagger (\hat{a}_{\mathbf{r},\downarrow} - i\hat{a}_{\mathbf{r},\uparrow}) + \text{H.c.},$$

$$\hat{H}_{\mathbf{ry}} = \hat{a}_{\mathbf{r-y},\uparrow}^\dagger (\hat{a}_{\mathbf{r},\downarrow} + i\hat{a}_{\mathbf{r},0}) - \hat{a}_{\mathbf{r+y},\uparrow}^\dagger (\hat{a}_{\mathbf{r},\downarrow} - i\hat{a}_{\mathbf{r},0}) + \text{H.c.},$$

$$(11)$$

where $\hat{H}_{\mathbf{rx}}$ and $\hat{H}_{\mathbf{ry}}$ represent the spin-flip hopping along the x and y axis with the tunneling amplitude t, respectively. $\hat{a}_{\mathbf{r},s}$ is the fermionic annihilation operator on site $\mathbf{r}$ for the spin state $|s\rangle$, and $\Gamma_0 = 2iM$ with the tunable parameter M is the strength of the on-site spin flip.

Under the periodic boundary condition, Hamiltonian (11) can be rewritten as

$$\hat{H}_{2D} = \sum_{\mathbf{k},ss'} \hat{a}_{\mathbf{k}s}^\dagger [\mathcal{H}(\mathbf{k})]_{ss'} \hat{a}_{\mathbf{k}s'},$$

where $\hat{a}_{\mathbf{k}s} = 1/\sqrt{V} \sum_{\mathbf{r}} e^{-i\mathbf{k}\cdot\mathbf{r}} \hat{a}_{\mathbf{r}s}$ is the annihilation operator in momentum space $\mathbf{k} = (k_x, k_y)$. The Bloch Hamiltonian $\mathcal{H}(\mathbf{k})$ has the form of Eq. (10), where the Bloch vector is given by

$$R_x = 2t \sin k_x,$$
$$R_y = 2t \sin k_y,$$
$$R_z = 2t(M - \cos k_x - \cos k_y), \qquad (12)$$

with the lattice spacing $a \equiv 1$ and $\hbar \equiv 1$ hereafter. The energy spectrum of this system is given by $E(\mathbf{k}) = 0, \pm|\mathbf{R}(\mathbf{k})|$, which has a zero-energy flat band in the middle of the three bands. In the following, we illustrate that this model has rich phase diagrams: it is a normal insulator for $|M| > 2$ with Chern number $\mathcal{C} = 0$; it is a topological insulator for $|M| < 2$ except for when $M = 0$ with Chern number $|\mathcal{C}| = 2$; it is a topological metal for $|M| = 2$ with a quantized Berry phase $|\gamma| = 2\pi$; it is a trivial metal for $M = 0$ with Berry phase $\gamma = 0$ (see Appendix B).

B. 2D Maxwell fermions in Maxwell metals

The three bands touch at a single point when M is -2 or 2, and touch at two points when M is zero. For $M = 2$, the three bands touch at $\mathbf{K}_+ = (0,0)$ in the energy spectrum shown in Fig. 1(a). We expand the Bloch Hamiltonian in the vicinity of the threefold degenerate point and obtain the following
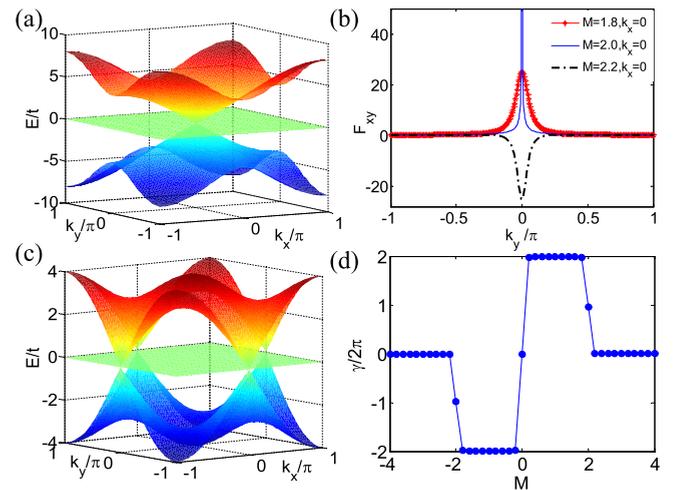

FIG. 1. (a) Energy spectrum for $M = 2$; (b) the Berry curvature $F_{xy}(k_y)$ for $k_x = 0$ and $M = 1.8, 2, 2.2$; (c) the energy spectrum for $M = 0$; (d) the Berry phase γ as a function of the parameter M, which corresponds to the Chern number $\mathcal{C}_1 = \gamma/2\pi$ when the 2D system is in the insulating phase with $M \neq 0, \pm 2$.

effective Hamiltonian for the low-energy excitations in the system

$$\mathcal{H}_+(\mathbf{q}) = vq_x\hat{S}_x + vq_y\hat{S}_y, \qquad (13)$$

where $v = 2t$ is the effective speed of light and $\mathbf{q} = \mathbf{k} - \mathbf{K}_+$. This effective Hamiltonian takes the Maxwell Hamiltonian $\hat{H}_M$ in Eq. (8) in 2D, and thus the dynamics of the low-energy excitations can be effectively described by the Maxwell equations. In this sense, we name these low-energy excitations Maxwell fermions and the threefold degeneracy point Maxwell point. When the Fermi level lies near the Maxwell point, the system can be named Maxwell metal, which is a metallic state due to the existence of the zero-energy flat band.

It is interesting to note that the Maxwell point in the 2D lattice system has topological stability characterized by a quantized Berry phase. To study the topological stability, we calculate the Berry phase for a Maxwell fermion circling around the Maxwell point

$$\gamma = \oint_c d\mathbf{k} \cdot \mathbf{F}(\mathbf{k}), \qquad (14)$$

where the Berry curvature $\mathbf{F}(\mathbf{k}) = \nabla \times \mathbf{A}(\mathbf{k})$ with the Berry connection defined by the wave function $|\psi_n(\mathbf{k})\rangle$ in the nth ($n = 1,2,3$) band $\mathbf{A}(\mathbf{k}) = -i\langle\psi_n(\mathbf{k})|\nabla_\mathbf{k}|\psi_n(\mathbf{k})\rangle$. For this three-band system described by the Bloch Hamiltonian $\mathcal{H}(\mathbf{k})$, the lowest-band Berry curvature in the k_x-k_y space can be rewritten as [27]

$$F_{xy} = -\frac{1}{R^3}\mathbf{R} \cdot \left(\partial_{k_x}\mathbf{R} \times \partial_{k_y}\mathbf{R}\right). \qquad (15)$$

The distributions $F_{xy}(k_y)$ for fixed $k_x = 0$ and typical parameters $M = 1.8, 2, 2.2$ are plotted in Fig. 1(b), and the results show that F_{xy} is a Dirac-δ function at the Maxwell point. The numerical integration of F_{xy} over the Brillouin zone for $M = 2$ gives the Berry phase $\gamma = 2\pi$, which is confirmed by analytical calculation. When $M = -2$, the single Maxwell point moves to the Brillouin edge $\mathbf{K}_- = (\pi,\pi)$ with a quantized Berry phase $\gamma = -2\pi$, and the low-energy effective Hamiltonian becomes $\mathcal{H}_-(\mathbf{q}) = -\mathcal{H}_+(\mathbf{q})$. When $M = 0$ and with the energy spectrum shown in Fig. 1(c), there are two Maxwell points at $(0,\pi)$ and $(\pi,0)$ with the effective Hamiltonian

$$\mathcal{H}_0(\mathbf{q}) = \pm vq_x\hat{S}_x \mp vq_y\hat{S}_y. \qquad (16)$$

In this case, the Berry phase for both Maxwell points is $\gamma = 0$, which corresponds to a trivial metallic state. So we can conclude that the single Maxwell point with linear dispersion relationship carrying a $\pm 2\pi$ Berry phase is a unique topological property of this 2D Maxwell metallic state, which is different from the Dirac points in monolayer or bilayer graphene [28].

C. Maxwell edge modes in Maxwell insulators

The system is an insulator when $M \neq 0, \pm 2$ since there is a gap between any two subbands. Under this condition, we can calculate the corresponding Chern number $\mathcal{C}_n$ for the three bands with the band index n:

$$\mathcal{C}_n = \frac{1}{2\pi}\int_{BZ} dk_x dk_y F_{xy}(k_x,k_y) = \gamma/2\pi. \qquad (17)$$
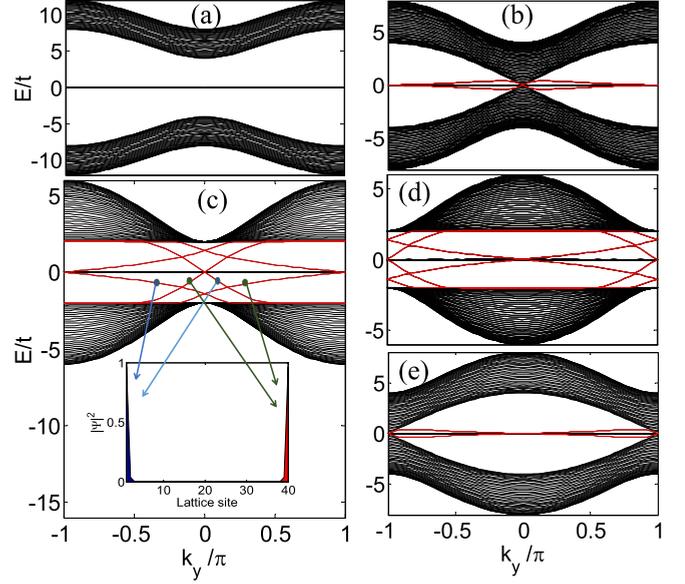

FIG. 2. Energy spectra and edge states in 2D lattices for (a) $M = 4$, (b) $M = 2$, (c) $M = 1$, (d) $M = -1$, and (e) $M = -2$. The inset in (c) shows the density distributions of four typical edge modes. The edge modes in (a)–(e) are plotted in red. The lattice site is $L_x = 40$ under the open boundary condition.

We find that nonzero Chern numbers $\mathcal{C}_1 = -\mathcal{C}_3 = 2\,\text{sgn}(M)$ for $|M| < 2$ and $\mathcal{C}_1 = \mathcal{C}_3 = 0$ for $|M| > 2$, and thus the zero Chern number $\mathcal{C}_2(M) = 0$ for the flat band (see Appendix B). Figure 1(d) shows the Berry phase of the lowest band $\gamma = 2\pi\mathcal{C}_1$ as a function of the parameter M, which indicates topological phase transition with band closing in this system when $M = -2, 0, 2$.

To further study the topological properties, we numerically calculate the energy spectrum of the system under the periodic boundary condition along the y direction and under the open boundary condition along the x direction with the length $L_x = 40$. The results in Fig. 2 show the variation of the energy spectra by changing the parameter M. For $M = 4$ [Fig. 2(a)], there is no edge mode between the two band gaps in this trivial insulating state with the Chern number $\mathcal{C}_n = 0$. When $|M|$ decreases to critical values $M = \pm 2$ [Figs. 2(b) and 2(e)], the band gaps close and the system is in the nontrivial Maxwell metallic phase with $\pm 2\pi$ Berry phase (corresponding to the Chern number ± 1) and a branch of edge modes connecting the lowest (third) band and the middle flat band. For $M = \pm 1$ [Figs. 2(c) and 2(d)], the spectra contain two pairs of asymmetric branches of edge modes connecting the lowest (third) band and the middle flat band, which is consistent with bulk-edge correspondence with the bulk Chern number $|\mathcal{C}_{1,3}| = 2$. The density distributions of some edge modes are shown in the inset of Fig. 2(c) for typical k_y.

The edge modes in the topological insulator phase have nontrivial properties. Without loss of generality, we explore the edge modes in the first band gap for parameter $M = 1$. We find a correspondence between the helicity of these edge states and the polarization of photons, so we named them Maxwell edge modes in this so-called Maxwell topological insulator. In particular, we reveal that this system exhibits the
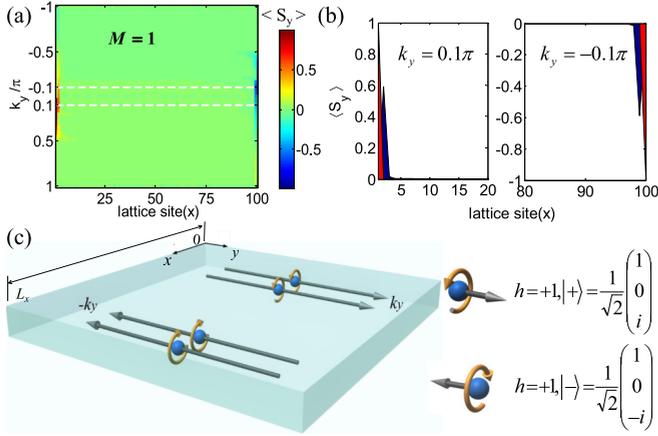
FIG. 3. (a) Expectation value of $\hat{S}_y$ as a function of k_y and x with lattice sites $L_x = 100$ under the open boundary condition; (b) density distribution of $\hat{S}_y(x)$ for $k_y = 0.1\pi$ and $k_y = -0.1\pi$; (c) schematic diagram for Maxwell edge states $|+\rangle$ and $|-\rangle$ in the Maxwell topological insulator with opposite momenta, both corresponding to the right circularly polarized photons with helicity $h = +1$.

analogous quantum anomalous Hall effect [29], with the edge modes being strong spin-momentum locking as eigenstates of the spin operator $\hat{S}_y$. This means that the two bunches of quasiparticle streams on the two edges (in the x direction) can be treated as the streams of polarized Maxwell quasiparticles moving along the y axis.

In Fig. 3(a), we numerically calculate the expectation value $\langle \hat{S}_y \rangle$ of the wave function with $L_x = 100$. The results show that the distribution of $\langle \hat{S}_y(k_y,x) \rangle$ has two peaks localized at both the left and right edges with an opposite sign. To be more precise, we plot $\langle \hat{S}_y(x) \rangle$ for $k_y = 0.1\pi$ and $k_y = -0.1\pi$ in Fig. 3(b), respectively. The result indicates that only the two edge states for each edge are the eigenstates of $\hat{S}_y$. The edge states on the left with positive eigenvalue are $|+\rangle = \frac{1}{\sqrt{2}}(1,0,i)^T = \frac{1}{\sqrt{2}}(\mathbf{e}_x + i\mathbf{e}_z)^T$, and the ones on the right edge with negative eigenvalue are $|-\rangle = \frac{1}{\sqrt{2}}(1,0,-i)^T = \frac{1}{\sqrt{2}}(\mathbf{e}_x - i\mathbf{e}_z)^T$, where $\mathbf{e}_j$ $(j = x,y,z)$ are the unit vectors of Cartesian coordinates. So the effective Hamiltonian of edge states is given by

$$H_{\text{edge}} = v_y k_y \hat{S}_y. \qquad (18)$$

This effective Hamiltonian is none other than the 1D Hamiltonian of circularly polarized photons. The helicity operator defined as

$$\hat{h} = \hat{\mathbf{S}} \cdot \frac{\mathbf{k}}{|\mathbf{k}|} = \text{sgn}(k_y)\hat{S}_y \qquad (19)$$

is the projection of the spin along the direction of the linear momentum [15]. Thus the edge quasiparticle streams in this Maxwell topological insulator can be treated as Maxwell fermion streams with the same helicities $h \equiv \langle \hat{h} \rangle = +1$ for opposite momenta, which satisfies the helicity conservation of massless photons in quantum field theory, as shown in Fig. 3(c). In addition, the momentum $\mathbf{k}$ can also be considered as the wave vector of the plane electromagnetic wave propagated along the y axis. Both edge states $|+\rangle$ $(k_y > 0)$ and $|-\rangle$ $(k_y < 0)$ with the same helicities can be regarded

as right circularly polarized waves which constitute the two independent transverse polarization vector $\mathbf{e}_x$ and $\mathbf{e}_z$ with opposite momenta. We can see from Fig. 3(c) that the Maxwell edge modes moving along the $+y$ $(-y)$ direction correspond to the right circularly polarized waves rotating counterclockwise (clockwise) in the xz plane (along the $-y$ axis) propagated along the $+y$ $(-y)$ direction. Likewise, when $-2 < M < 0$ with $\mathcal{C} = -2$, the Maxwell edge modes on the left (right) edge with $h = -1$ correspond to the left circularly polarized waves propagated along the $-y$ $(+y)$ direction. Because the electromagnetic waves are transverse waves, there is no longitudinal component and no edge mode with helicity $h = 0$, which corresponds to the unit wave vector of plane waves. So, our Maxwell edge modes with strong spin-momentum locking correspond perfectly to the circularly polarized photons.

IV. MAXWELL FERMIONS IN 3D LATTICE SYSTEMS

In this section, we generalize the proposed model and results of Maxwell fermions to the 3D lattice system. We first construct a 3D lattice model by adding a spin-flip hopping term along the z axis into the previous 2D model Hamiltonian in Eq. (11), and then study the topological properties of the Maxwell fermions near the 3D Maxwell points.

A. 3D model

The generalized 3D tight-binding model on a simple cubic lattice Hamiltonian is given by

$$\hat{H}_{3D} = \hat{H}_{2D} + t\sum_{\mathbf{r}} \hat{H}_{\mathbf{rz}},$$

$$\hat{H}_{\mathbf{rz}} = -i(\hat{a}^\dagger_{\mathbf{r+z},0}\hat{a}_{\mathbf{r},\uparrow} + \hat{a}^\dagger_{\mathbf{r},0}\hat{a}_{\mathbf{r+z},\uparrow}) + \text{H.c.}, \qquad (20)$$

where $\hat{H}_{\mathbf{rz}}$ is the additional hopping term along the z axis. The Bloch Hamiltonian of the 3D system takes the same form as Eq. (10), and the Bloch vectors $\mathbf{R}(\mathbf{k})$ with $\mathbf{k} = (k_x,k_y,k_z)$ are given by

$$R_x = 2t \sin k_x, \quad R_y = 2t \sin k_y,$$

$$R_z = 2t(M - \cos k_x - \cos k_y - \cos k_z). \qquad (21)$$

One can check that the spin-1 matrices satisfy the following relationship under the inversion operation $\hat{P}$ and the time-reversal operation $\hat{T}$:

$$\hat{P}\hat{S}_x\hat{P}^{-1} = -\hat{S}_x, \quad \hat{T}\hat{S}_x\hat{T}^{-1} = -\hat{S}_x,$$

$$\hat{P}\hat{S}_y\hat{P}^{-1} = -\hat{S}_y, \quad \hat{T}\hat{S}_y\hat{T}^{-1} = -\hat{S}_y,$$

$$\hat{P}\hat{S}_z\hat{P}^{-1} = \hat{S}_z, \quad \hat{T}\hat{S}_z\hat{T}^{-1} = -\hat{S}_z, \qquad (22)$$

where $\hat{P} = \text{diag}(1,1,-1)$ and $\hat{T} = \hat{I}\hat{K}$ with $\hat{I} = \text{diag}(1,1,1)$ and $\hat{K}$ being the complex conjugate operator. Thus the Bloch Hamiltonian has an inversion symmetry represented by

$$\hat{P}\mathcal{H}(\mathbf{k})\hat{P}^{-1} = \mathcal{H}(-\mathbf{k}), \qquad (23)$$

but it does not have the time-reversal symmetry since

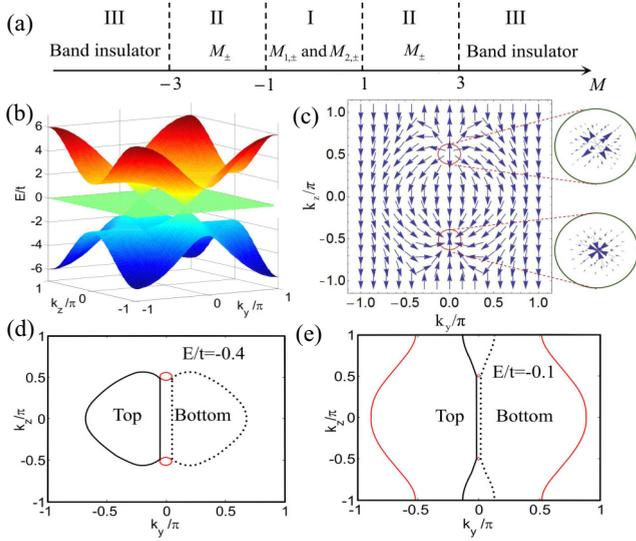$$\hat{T}\mathcal{H}(\mathbf{k})\hat{T}^{-1} \neq \mathcal{H}(-\mathbf{k}). \qquad (24)$$

FIG. 4. (a) Phase diagrams with regimes I, II, III denote two pairs of Maxwell points $M_{1,\pm}$ and $M_{2,\pm}$, one pair of Maxwell points $M_\pm$, and normal band insulators, respectively. (b) The energy spectrum as a function of k_y and k_z for $k_x = 0$; (c) the vector distribution of the Berry curvature $\mathbf{F(k)}$ at the $k_x = 0$ plane. The figures in the red circles show $\mathbf{F(k)}$ around the Maxwell points as a sink or source in momentum space; (d) and (e) show Fermi arcs appear at $E/t = -0.4$ and $E/t = -0.1$ under the open boundary condition along the x direction, respectively. The two black solid lines on the left represent two Fermi arcs connecting the two red circles which are the bulk states near the Maxwell points with opposite monopole charges at the top surface. The two black dot lines on the right represent Fermi arcs in the bottom surface. The two red lines in (e) also denote bulk states. The parameter in (b)–(e) is $M = 2$.

In this system, the Maxwell points can be manipulated through the tunable parameter M. The phase diagram with respect to M is shown in Fig. 4(a): the system is a Maxwell metal for $|M| < 3$, while it is a normal insulator for $|M| > 3$. Moreover, there are two pairs of Maxwell points denoted by $\mathbf{M}_{1,\pm} = (0,\pi, \pm \arccos M)$ and $\mathbf{M}_{2,\pm} = (\pi,0, \pm \arccos M)$ for $0 \leqslant |M| < 1$; there are a single pair of Maxwell points at $\mathbf{M}_\pm = [0,0, \pm \arccos(M - 2)]$ ($\mathbf{M}_\pm = [\pi,\pi, \pm \arccos(M + 2)]$) for $1 < M < 3$ ($-3 < M < -1$). At the critical points of $M = \pm3$, the two Maxwell points merge and then disappear by opening a gap when $|M| > 3$, corresponding to the normal insulating phase.

The three bands $E(\mathbf{k}) = 0, \pm |\mathbf{R(k)}|$ can touch at certain points to form threefold degeneracy points under the condition of $|M| \leqslant 3$. Considering the typical case of $M = 2$, we find that the band spectrum hosts two threefold degeneracy points in the first Brillouin zone at $\mathbf{M}_\pm = (0,0,\pm\frac{\pi}{2})$, as shown in Fig. 4(b). The low-energy effective Hamiltonian now becomes

$$\mathcal{H}_{M_\pm}(\mathbf{q}) = vq_x \hat{S}_x + vq_y \hat{S}_y \pm vq_z \hat{S}_z, \quad (25)$$

where $v = 2t$ is the effective speed of light. This Hamiltonian takes the form of the isotropic 3D Maxwell Hamiltonian in Eq. (8), and thus these low-energy excitations are named 3D Maxwell fermions.

B. Topological properties

To further study the topological properties of the 3D Maxwell fermions, we plot the vector distribution of the Berry curvature $\mathbf{F(k)}$ at the $k_x = 0$ plane in Fig. 4(c). One can find that the Maxwell points $\mathbf{M}_\pm = (0,0, \pm \frac{\pi}{2})$ behave as a sink and source of the Berry flux [see the 3D distribution of $\mathbf{F(k)}$ near the two points]. Thus the Maxwell points behave like magnetic monopoles in the momentum space with topological charges defined by the Chern numbers (see Appendix B)

$$\mathcal{C}_{M_\pm} = \frac{1}{2\pi} \oint_S d\mathbf{k} \cdot \mathbf{F(k)} = \pm 2, \quad (26)$$

which is twice that of a Weyl point in Weyl semimetals. Once we fix k_z as a parameter, $\mathcal{H}_{k_z}(k_x,k_y)$ can be viewed as a 2D Maxwell insulator, with the k_z-dependent Chern number $\mathcal{C}_{k_z} = 2$ when $k_z \in (-\frac{\pi}{2},\frac{\pi}{2})$ and $C_{k_z} = 0$ when otherwise. So there are always two Fermi arcs of surface states connecting a pair of Maxwell points with opposite topological charges, as shown in Figs. 4(d) and 4(e), in contrast to one Fermi arc [3,4,6,7] in Weyl semimetals. Here the surface and bulk states are plotted in black and red, and the surface states that lie at the top and bottom surfaces along the x direction are respectively denoted by solid and dot lines. It is interesting to note that the Fermi-arc surface states in this Maxwell metal diffuse to the bulk states due to the zero-energy flat band, which leads to nonzero energy Fermi arcs. In addition, the 3D Maxwell points in Maxwell metals have linear momenta along all three directions, in contrast to the quadratic form of double-Weyl points [30].

We can change the positions of the Maxwell points inside the Brillouin zone by changing the parameter M. Without loss of generality, we discuss the merging process of the Maxwell points for $M > 0$. For $M = 0$, there are two pairs of Maxwell points at $\mathbf{M}_{1,\pm} = (0,\pi, \pm \frac{\pi}{2})$ and $\mathbf{M}_{2,\pm} = (\pi,0, \pm \frac{\pi}{2})$ with monopole charges ∓2, as shown in Fig. 5(a). The two pairs of Maxwell points move together along the k_z axis as we increase the parameter M. They then emerge at $(0,\pi,0)$ and $(\pi,0,0)$, respectively, with a monopole charge of zero for $M = 1$. Meanwhile, there are another pair of Maxwell points both with a monopole charge of zero created at $(0,0, \pm \pi)$, as shown in Fig. 5(b). When we continuously increase M, two Maxwell points located at $(0,\pi,0)$ and $(\pi,0,0)$ disappear by opening gaps, and the single pair of Maxwell points denoted by $\mathbf{M}_\pm = [0,0, \pm \arccos(M - 2)]$ move to the $(0,0,0)$ point with a monopole charge of ±2, with the typical case for $M = 2$ shown in Fig. 5(c). At the critical point $M = 3$ in Fig. 5(d), the two Maxwell points with opposite monopole charges emerge at $(0,0,0)$ and then disappear by opening gaps when $M > 3$.

Finally, in this section, we briefly discuss the topological stability of the 3D Maxwell points. Unlike Weyl points that are strongly robust [31], Maxwell points can only be stabilized by certain symmetry. In our proposed lattice systems, the band gaps will be opened and thus Maxwell points are gapped when the inversion symmetry is broken by introducing a perturbation term with one of the other five Gell-Mann matrices. This is due to the fact that the Maxwell Hamiltonian only takes three of the eight Gell-Mann matrices. So the topological stability of Maxwell points are weaker than Weyl points. However,
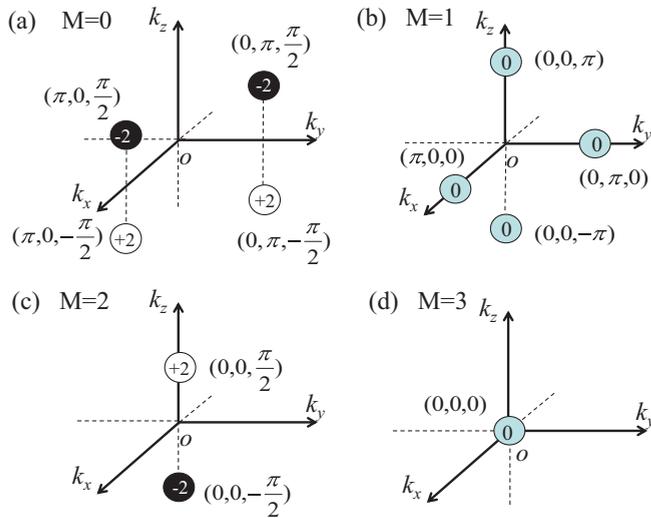
FIG. 5. Merging of 3D Maxwell points. (a) When $M = 0$, two pairs of Maxwell points locate at $(0,\pi, \pm \frac{\pi}{2})$ and $(\pi,0, \pm \frac{\pi}{2})$ with a monopole charge of ∓ 2. (b) When $M = 1$, four Maxwell points appear at $(0,\pi,0)$, $(\pi,0,0)$, and $(0,0, \pm \pi)$ with a zero monopole charge. (c) Typical case of $M = 2$, where there are two Maxwell points located at $(0,0, \pm \frac{\pi}{2})$ with a monopole charge of ± 2. (d) Critical point when $M = 3$. The two Maxwell points with opposite monopole charges emerge at $(0,0,0)$ and then disappear by opening band gaps for $M > 3$.

Maxwell points would still be stable as long as the system is protected by certain symmetry, such as the inversion symmetry

in our 3D system. In this case, the perturbations under the same symmetry would not open the band gaps and only change the positions of Maxwell points in the Brillouin zone (see Fig. 5) until the topological phase transition occurs.

V. PROPOSAL FOR EXPERIMENTAL REALIZATION AND DETECTION

Now we proceed to propose a realistic scheme for realizing the 2D and 3D model Hamiltonians with ultracold atoms in the square and cubic optical lattices by using the Raman-assisted tunneling method [32–38], respectively. We also suggest that the Chern numbers can be revealed from the shift of the hybrid Wannier center of an atomic cloud, based on a generalization of topological pumping in the optical lattices [39–45].

A. Proposed realization in optical lattices

To realize the 2D model Hamiltonian in Eq. (11), we consider noninteracting atoms in a titled square optical lattice with the lattice spacing a and choose three atomic internal states in the ground-state manifold to carry the spin states, as shown Fig. 6(a). The other levels in the ground-state manifold are irrelevant as they can be depopulated by the optical pumping. The on-site spin-flip term $\Gamma_0 \hat{a}_{\mathbf{r},0}^{\dagger} \hat{a}_{\mathbf{r},\uparrow}$ can be easily achieved by applying a radio-frequency field or Raman beams for coupling the atomic internal states $|\uparrow\rangle$ and $|0\rangle$. The major difficulty for implementing our model is to realize the spin-flip hopping terms $\hat{H}_{\mathbf{r}x}$ and $\hat{H}_{\mathbf{r}y}$ along each direction. By
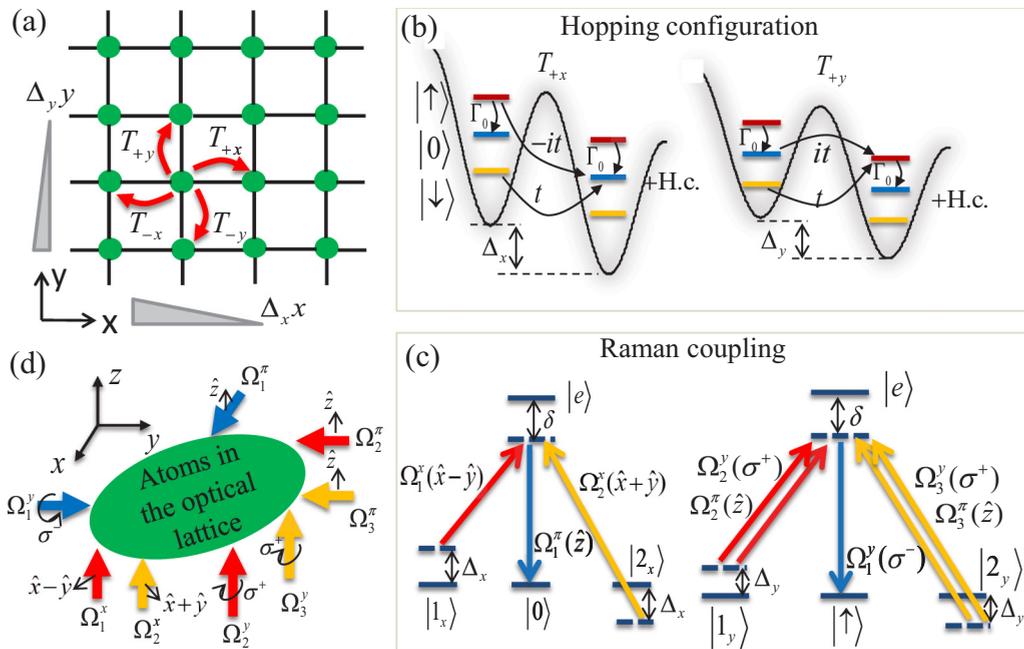

FIG. 6. Scheme for realizing the 2D model Hamiltonian. (a) Schematic diagram of the square optical lattice and the atomic hopping along the two axis denoted by $T_{\pm x}$ and $T_{\pm y}$. (b) The atomic hopping configuration in the 2D model Hamiltonian in Eq. (11). The three atomic internal states $|\uparrow\rangle,|0\rangle,|\downarrow\rangle$ form the (pseudo)spin-1 basis, such that $T_{\pm(x,y)}$ represents spin-flip hopping and the Γ_0 term represents on-site spin flip. A large linear tilt $\Delta_{x,y}$ per lattice site along x,y direction is used to suppress the natural hopping and the hopping can then be restored by Raman lasers. (c) The Raman coupling scheme for engineering the required spin-flip hopping along each axis. The detuning in each direction matches the frequency offset of the corresponding Raman beams. (d) The Raman lasers with the corresponding polarization and propagation direction.

defining the superposition states

$$|1_x\rangle = (|\downarrow\rangle - i|\uparrow\rangle)/\sqrt{2}, \quad |2_x\rangle = (|\downarrow\rangle + i|\uparrow\rangle)/\sqrt{2},$$
$$|1_y\rangle = (|\downarrow\rangle - i|0\rangle)/\sqrt{2}, \quad |2_y\rangle = (|\downarrow\rangle + i|0\rangle)/\sqrt{2}, \quad (27)$$

the two hopping terms can be diagrammatically visualized as

$$T_x = T_{+x} + T_{-x}$$
$$= \overset{\times}{\curvearrowright} |1_x\rangle \overset{\sqrt{2}}{\curvearrowright} |0\rangle + |0\rangle \overset{-\sqrt{2}}{\curvearrowright} |2_x\rangle \overset{\times}{\curvearrowright} + \text{H.c.},$$
$$T_y = T_{+y} + T_{-y}$$
$$= \overset{\times}{\curvearrowright} |1_y\rangle \overset{-\sqrt{2}}{\curvearrowright} |\uparrow\rangle + |\uparrow\rangle \overset{\sqrt{2}}{\curvearrowright} |2_y\rangle \overset{\times}{\curvearrowright} + \text{H.c.}, \quad (28)$$

where $\overset{\times}{\curvearrowright}$ indicates that the hopping is forbidden along this direction. The hopping terms T_{+x} and T_{+y} are shown in Fig. 6(b), which can be realized by using the Raman-assisted tunneling with proper laser-frequency and polarization selections [32–38]. First, the required broken parity (left-right) symmetry is achieved by titling the lattice with a homogeneous energy gradient along the two directions, which can be created by the gravitational field or the gradient of a dc- or ac-Stark shift. Here we require different linear energy shifts per site $\Delta_{x,y}$ along different directions, such as $\Delta_x = 1.5\Delta_y$. Then the natural hopping is suppressed by the large tilt potential, and the hopping terms are restored and engineered by applying two-photon Raman coupling with the laser beams of proper configurations [see Fig. 6(c)].

We consider the realization of the hopping term $\hat{H}_{\mathbf{rx}}$ to explain the Raman scheme, and first focus on the single term $T_{+x}^{(1)} = \hat{a}_{\mathbf{r+x},0}^\dagger(\hat{a}_{\mathbf{r},\downarrow} - i\hat{a}_{\mathbf{r},\uparrow})$ (here $T_{+x} = T_{+x}^{(1)} + \text{H.c.}$) for details. This term corresponds to an atom in the spin state $|1_x\rangle = (|\downarrow\rangle - i|\uparrow\rangle)/\sqrt{2}$ at site $\mathbf{r}$ hopping to site $\mathbf{r + x}$ while changing the spin state to $|0\rangle$ with hopping strength $\sqrt{2}t$, which can be visualized as $\overset{\times}{\curvearrowright} |1_x\rangle \overset{\sqrt{2}}{\curvearrowright} |0\rangle$. This hopping term can be achieved by two Raman beams $\Omega_1^x(\hat{x} - \hat{y}) = \sqrt{2}\Omega_0 e^{ikz}$ polarized along $(\hat{x} - \hat{y})$ direction and $\Omega_1^\pi(\hat{z}) = \Omega_0 e^{ikx}$ with π polarization along $\hat{z}$ direction. Here the population of the excited state $|e\rangle$ which is estimated by $|\Omega_0/\delta|^2$ is negligible due to the large single-photon detuning δ. The two-photon detuning Δ_x matching the linear energy shift of the lattice per site ensures that it only allows $|1_x\rangle$ hopping to the right, and the other direction is forbidden by a large energy mismatch $2\Delta_x$. We can address the spin states through the polarization selection rule since the original spin basis $|\downarrow\rangle,|0\rangle,|\uparrow\rangle$ differs in the magnetic quantum number by one successively. Thus a π-polarized beam Ω_1^π excites the state $|0\rangle$ and a linear $(\hat{x} - \hat{y})$-polarized beam Ω_1^x excites the superposition state $|1_x\rangle = (|\downarrow\rangle - i|\uparrow\rangle)/\sqrt{2}$ as the polarization $(\hat{x} - \hat{y}) \sim (\sigma^+ - i\sigma^-)$. These two beams together induce a Raman-assisted hopping between $|1_x\rangle$ and $|0\rangle$. The hopping amplitude and phase are controlled by the corresponding Raman beam amplitude and phase [32–38], which can be written as

$$t_{\mathbf{r},+\mathbf{x}} = \frac{\sqrt{2}|\Omega_0|^2}{\delta}\beta\, e^{i\delta\mathbf{k}\cdot\mathbf{r}},$$
$$\beta = \int dx\, w^*(x+a)e^{-ikx}w(x)\int dy\, w^*(y)w(y). \quad (29)$$

Here $\delta\mathbf{k} = (-k,0)$ and we have used factorization of the Wannier function $w(\mathbf{r}') = w(x')w(y')$ in the square lattice. If we adjust the interfering angle of the lattice beams to satisfy the condition $ka = 2\pi$, the site dependent phase term can always be reduced to $e^{i\delta\mathbf{k}\cdot\mathbf{r}} = 1$. In this case, we can obtain the required hopping strength $t_x = \sqrt{2}t$ with $t = \beta|\Omega_0|^2/\delta$. We note that these two Raman lasers simultaneously induce the Hermitian conjugate process of the hopping $T_{+x}^{(1)}$, which is the desired spin-flip tunneling from $|0\rangle$ to $|1_x\rangle$ along the $+x$ direction. Similarly, the second hopping term T_{-x} can be realized by the two Raman beams $\Omega_1^\pi(\hat{z}) = \Omega_0 e^{ikx}$ and $\Omega_2^x(\hat{x} + \hat{y}) = -\sqrt{2}\Omega_0 e^{ikz}$ polarized along $(\hat{x} + \hat{y})$ direction, which couple the state $|0\rangle$ and $|2_x\rangle$ since $(\hat{x} + \hat{y}) \sim (\sigma^+ + i\sigma^-)$. Thus the hopping along the x axis can thus be realized by three Raman beams with the configuration shown in Fig. 6(c).

The hopping terms $\hat{H}_{\mathbf{ry}}$ along the y axis can be realized in a similar way. Along this direction, the hopping term $T_{+y} = -\hat{a}_{\mathbf{r+y},\uparrow}^\dagger(\hat{a}_{\mathbf{r},\downarrow} - i\hat{a}_{\mathbf{r},0}) + \text{H.c.}$ can be realized by three Raman beams $\Omega_1^y(\sigma^-) = \Omega_0 e^{iky}$, which excites the state $|\uparrow\rangle$, and $\Omega_2^y(\sigma^+) = -\sqrt{2}\Omega_0 e^{ikz}$ and $\Omega_2^\pi(\hat{z}) = i\sqrt{2}\Omega_0 e^{-iky}$, which together effectively excite the state $|1_y\rangle = (|\downarrow\rangle - i|0\rangle)/\sqrt{2}$. The hopping term $T_{-y} = \hat{a}_{\mathbf{r-y},\uparrow}^\dagger(\hat{a}_{\mathbf{r},\downarrow} + i\hat{a}_{\mathbf{r},0}) + \text{H.c.}$ can be realized by two additional Raman beams $\Omega_3^y(\sigma^+) = \sqrt{2}\Omega_0 e^{ikz}$ and $\Omega_3^\pi(\hat{z}) = i\sqrt{2}\Omega_0 e^{-iky}$ which effectively excite the state $|2_y\rangle = (|\downarrow\rangle + i|0\rangle)/\sqrt{2}$. Here a wave-vector difference $\delta\mathbf{k}' = (0, -2k)$ leads to the same hopping strength $t_y = t_x$ along this axis. The laser configurations for realizing the desired hopping terms along the y axis are also shown in Fig. 6(c). The total laser beams with the polarization and propagation directions for realizing all the hopping terms in the 2D model Hamiltonian in Eq. (11) are shown in Fig. 6(d). Note that the detuning in each direction matches the frequency offset of the corresponding Raman beams. It is also important to forbid the undesired tunneling terms that require different linear energy shifts per site along the two axis, which can be achieved by adjusting the direction of the gradient field to be in different angles with respect to the axes of the square optical lattice.

The proposed Raman scheme can be directly extended to realize the 3D model Hamiltonian in Eq. (20). In this case, one can prepare the noninteracting atoms in a titled cubic optical lattice, as shown in Fig. 7(a). Here we require different linear
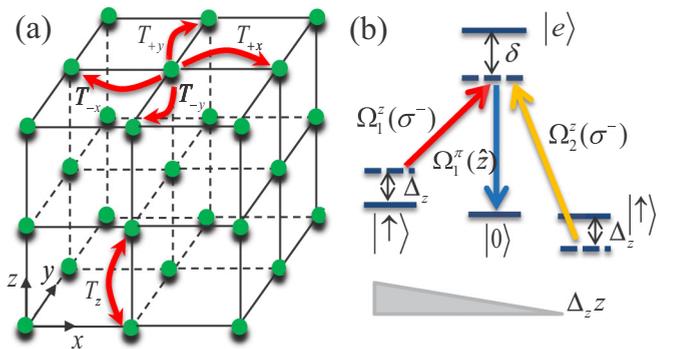

FIG. 7. (a) Schematic diagram of the simple cubic optical lattice and the atomic hopping. (b) The Raman coupling for realizing the hopping term T_z along the z axis.

energy shifts per site $\Delta_{x,y,z}$ along different directions, such as $\Delta_x = 1.5\Delta_y = 2\Delta_z$. The additional hopping $\hat{H}_{\mathbf{rz}}$ along the z axis can be implemented with the similar Raman coupling. Along the z axis, the hopping term can be diagrammatically visualized as

$$T_z = \overset{\times}{\curvearrowright} |\uparrow\rangle \overset{-i}{\curvearrowright} |0\rangle + |0\rangle \overset{-i}{\curvearrowright} |\uparrow\rangle \overset{\times}{\curvearrowright} + \text{H.c.} \qquad (30)$$

Combined with the laser Ω_1^π that couples the state $|0\rangle$, two additional Raman beams $\Omega_1^z(\sigma^-) = -i\Omega_0 e^{ikz}$ and $\Omega_2^z(\sigma^-) = -i\Omega_0 e^{-ikz}$ that couple the state $|\uparrow\rangle$ can be used to induce the hopping $\overset{\times}{\curvearrowright} |\uparrow\rangle \overset{-i}{\curvearrowright} |0\rangle$ and $|0\rangle \overset{-i}{\curvearrowright} |\uparrow\rangle \overset{\times}{\curvearrowright}$, respectively. The laser configurations for realizing the desired hopping term along the z axis are shown in Fig. 7(b), and thus all the hopping terms along each direction in the 3D model Hamiltonian can be realized.

Although the implementation of the 2D and 3D model Hamiltonians involves a number of Raman beams, all of the lasers can be drawn from the same one with the small relative frequency shift induced by an acoustic optical modulator. In addition, one can lock the relative frequency differences of these beams by the driving fields of the modulator such that the absolute frequencies and their fluctuations are not important. In typical experiments, for instance, by using ^{40}K atoms of mass m in an optical lattice with the lattice constant $a = 2\pi/k = 764$ nm, the gravity induces a potential gradient per lattice site $\Delta = mga/\hbar \approx 2\pi \times 0.75$ kHz. Gravity can provide the required gradients along three directions with an appropriate choice of the relative axes of the frame to satisfy $\Delta_z : \Delta_y : \Delta_x = 1 : 1.5 : 2$ and $\Delta = \sqrt{\Delta_x^2 + \Delta_y^2 + \Delta_z^2}$, such that $\Delta_z \approx 2\pi \times 1$ kHz. For a lattice with potential depth $V_0 \approx 20E_r$, where $E_r = \hbar^2 k^2/2m$ is the recoil energy, the overlap ratio $\beta \approx 0.01$, and the natural tunneling rate $t_N/\hbar \sim 10^{-3}E_r/\hbar \approx 2\pi \times 8.5$ Hz. For Raman beams with $\Omega_0/2\pi \approx 130$ MHz and the single-photon detuning $\delta/2\pi \approx 1.7$ THz, one has $|\Omega_0|^2/\delta \approx 2\pi \times 10$ kHz and the Raman-assisted hopping rate $t/\hbar \approx 2\pi \times 0.1$ kHz. Thus the population of the excited state $|e\rangle$ which is estimated by $|\Omega_0/\delta|^2$ is negligible due to the large single-photon detuning δ. During the typical experimental time of the order of $10/t$, the undesired off-resonant hopping probabilities with upper bounded by $t_N^2/\Delta_x^2 \sim 0.01$ and the effective spontaneous emission rate estimated by $|\Omega_0/\delta|^2\Gamma_s$ with the decay rate of the excited state $\Gamma_s \approx 2\pi \times 6$ MHz would be negligible [38]. We note that using several Raman lasers will lead to considerable heating effects in realistic experiments [37], which is the main disadvantage in our proposal. The cold-atom system can be effectively described by the proposed model Hamiltonian as long as the duration of an experiment is short compared to the heating time (the typical lifetime of an atomic gas), which is about 100 ms in experiments containing the heating induced by the Raman couplings [35,37].

B. Proposed detections

The 2D and 3D Maxwell points in the band structures that have related topological phase transition can be detected by the Bragg spectroscopy or Bloch-Zener oscillations, similar to the methods used for detecting Dirac and Weyl points in optical lattices [18–20,24]. In addition, the Berry curvature and thus

the quantized Berry phases and the Chern numbers can be measured by the newly developed technique of tomography of Bloch bands in optical lattices [46,47], and the Chern numbers can also be revealed from the shift of an atomic cloud's center of mass [48]. Below we propose that the Chern numbers can also be revealed from the shift of the hybrid Wannier center of an atomic cloud, based on a generalization of topological pumping in optical lattices [39–45].

The 2D Maxwell insulator can be viewed as a fictitious one-dimensional insulator subjected to an external parameter k_y by using the dimension reduction method [42]. Thus its Chern number can be defined by the polarization

$$P = \frac{1}{2\pi} \int_{-\pi}^{\pi} \mathbf{A}(\mathbf{k}) dk_x \qquad (31)$$

for the geometry of the underlying band structure. According to the modern theory of polarization, the Chern number defined in k_x-k_y space can be obtained from the change in polarization induced by adiabatically changing the parameter k_y by 2π:

$$\mathcal{C} = \int_{-\pi}^{\pi} \frac{\partial P(k_y)}{\partial k_y} dk_y. \qquad (32)$$

For measuring $P(k_y)$, one can use another fact that the polarization can alternatively be written as the center of mass of the Wannier function constructed for the single occupied band. In this system, the polarization $P(k_y)$ can be expressed by means of the centers of the hybrid Wannier functions, which are localized in the x axis retaining Bloch character in the k_y dimension. The variation of the polarization and thus the Chern number are directly related to the shift of the hybrid Wannier center along the x axis in the lattice. The shift of hybrid Wannier center by adiabatically changing k_y is proportional to the Chern number, which is a manifestation of topological pumping with k_y being the adiabatic pumping parameter

In the 2D lattice system, to construct and calculate the hybrid Wannier center, we can consider the Bloch Hamiltonian with parameter k_y and recover it to the tight-binding Hamiltonian along the x axis. The hybrid Wannier center can be written as [42]

$$\langle n_x(k_y) \rangle = \frac{\sum_{i_x} i_x \rho(i_x, k_y)}{\sum_{i_x} \rho(i_x, k_y)}, \qquad (33)$$

where $\rho(i_x, k_y)$ is the density distribution of hybrid Wannier center and denotes the atomic densities resolved along the x direction as a function of k_y. The density distribution can be written as

$$\rho(i_x, k_y) = \sum_{\text{occupied states}} \langle i_x, k_y | i_x, k_y \rangle, \qquad (34)$$

where $|i_x, k_y\rangle$ is the hybrid eigenstate of the system. In cold-atom experiments, the atomic density distribution $\rho(i_x, k_y)$ can be directly measured by the hybrid time-of-flight images, which is referring to an *in situ* measurement of the density distribution of the atomic cloud in the x direction during free expansion along the y direction. In the measurement, the optical lattice is switched off along the y and z directions while keeping the system unchanged in the x direction. One can map out the crystal momentum distribution along k_y in the time-of-flight images and a real space density resolution
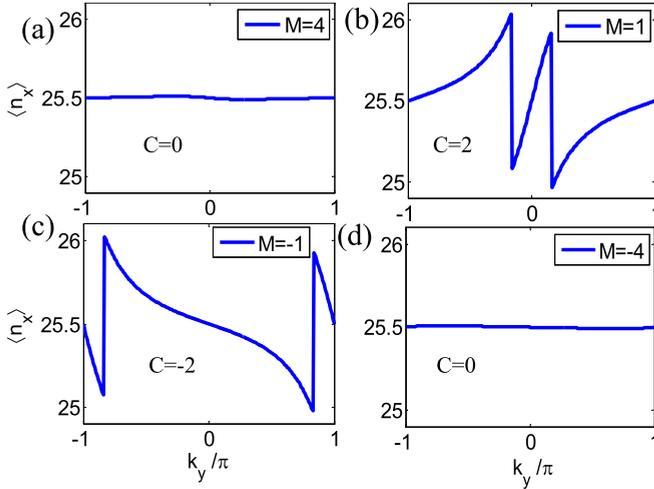
FIG. 8. Hybrid Wannier centers in a tight-binding chain of length $L_x = 50$ at 1/3 filling as a function of the adiabatic pumping parameter k_y for different parameters M. (a),(d) Without jump of $\langle n_x(k_y) \rangle$, which is consistent with the expected Chern number of the lowest band $\mathcal{C} = 0$ for $M > 2$ and $M < -2$ in the 2D trivial insulator phase. In (b) and (c), $\langle n_x(k_y) \rangle$ both show the jump of a two unit cell for $M = 1$ and $M = -1$, corresponding to the nontrivial Maxwell insulator phase with $\mathcal{C} = 2$ and $\mathcal{C} = -2$, respectively.
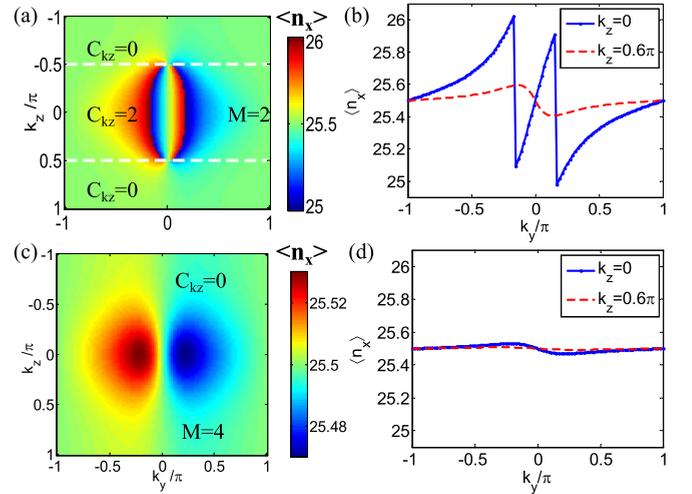

FIG. 9. Hybrid Wannier centers in a tight-binding chain of length $L_x = 50$ at 1/3 filling as a function of the adiabatic pumping parameter k_y for different parameters M and k_z. (a) The profile $\langle n_x(k_y, k_z) \rangle$ for the parameter $M = 2$, where $\langle n_x(k_y) \rangle$ (do not) shows double jumps in one unit cell for k_z (outside) within the region $(-\frac{\pi}{2}, \frac{\pi}{2})$, with typical examples shown in (b). (c) The profile $\langle n_x(k_y, k_z) \rangle$ for $M = 4$ shows no jump of $\langle n_x(k_y) \rangle$ for the whole k_z regime, with typical examples shown in (d). The corresponding k_z-dependent Chern number $\mathcal{C}_{k_z}$ is also plotted both in (a) with the white dashed lines denoting the critical value between the trivial regimes with $\mathcal{C}_{k_z} = 0$ and nontrivial regimes with $\mathcal{C}_{k_z} = 2$.

in the x direction can be done at the same time. Thus one can directly extract Chern number from this hybrid time-of-fight image in the cold-atom system.

We perform numerical simulations to demonstrate the feasibility of the detection scheme. We numerically calculate $\langle n_x(k_y) \rangle$ in a tight-binding chain of length $L_x = 50$ at 1/3 filling (assuming the Fermi energy $E_F = 0$), and the results for typical parameters are shown in Fig. 8. For the case in Figs. 8(a) and 8(d) when $M = 4$ and $M = -4$, respectively, $\langle n_x(k_y) \rangle$ shows no jump, which is consistent with the expected Chern number of the lowest band $\mathcal{C} = 0$ for the trivial cases. The results for $M = 1$ in Fig. 8(b) show two discontinuous jumps of one unit cell, indicating that a particle is pumped across the system [40,41], the Chern number of the lowest band for this case is $\mathcal{C} = 2$, and the result in Fig. 8(c) is similar to Fig. 8(b) but with the opposite jump direction, indicating $\mathcal{C} = -2$ when $M = -1$. This establishes a direct and clear connection between the shift of the hybrid density center and the topological invariant.

This method can be extended to detect the 3D Maxwell system. The 3D system can be further treated as a collection of k_z-modified 2D trivial or nontrivial Maxwell insulators with the k_z-dependent Chern number $\mathcal{C}_{k_z}$ defined in the k_x-k_y plane as different slices of out-of-plane quasimomentum k_z:

$$\mathcal{C}_{k_z} = \int_{-\pi}^{\pi} \frac{\partial P(k_y, k_z)}{\partial k_y} dk_y, \tag{35}$$

with the modified polarization $P(k_y, k_z)$ for the reduced one-dimensional insulators. In this case, the corresponding hybrid Wannier center is given by

$$\langle n_x(k_y, k_z) \rangle = \frac{\sum_{i_x} i_x \rho(i_x, k_y, k_z)}{\sum_{i_x} \rho(i_x, k_y, k_z)}, \tag{36}$$

which can also be measured by the hybrid time-of-flight images. The typical numerical results of $\langle n_x(k_y, k_z) \rangle$ in a tight-binding chain of length $L_x = 50$ at 1/3 filling are shown in Fig. 9. For $M = 2$ in Figs. 9(a) and 9(b), the two 3D Maxwell points at $k_z = \pm \frac{\pi}{2}$ separate the band insulators with $\mathcal{C}_{k_z} = 0$ and the topological insulators with $\mathcal{C}_{k_z} = 2$. As shown in Fig. 9(a), the hybrid Wannier center $\langle n_x(k_y) \rangle$ exhibits two discontinuous jumps of one unit cell within the region $k_z \in (-\frac{\pi}{2}, \frac{\pi}{2})$ and the jumps disappear outside this region. To show this more clearly, we plot $\langle n_x(k_y) \rangle$ for $k_z = 0$ and $k_z = 0.6\pi$ as two examples in Fig. 9(b). The double one-unit-cell jumps driven by k_y indicate that two particles are pumped across the system, as expected for $\mathcal{C}_{k_z} = 2$. For comparisons, we also show the results of $\langle n_x(k_y) \rangle$ for $M = 4$ without jump for all k_z regimes in Figs. 9(c) and 9(d), which is consistent with the expected $\mathcal{C}_{k_z} = 0$ when $M > 3$ for the band insulators.

VI. DISCUSSION AND CONCLUSION

The properties of the topological Maxwell quasiparticles that are analogous to the Dirac and Weyl fermions can be further investigated, for example, the relativistic wave dynamics with Klein tunneling [49] and Zitterbewegung oscillations [50], and the unconventional transport properties [51]. All of these properties can have unique features. For instance, there is one oscillation frequency in the Zitterbewegung effects of the Dirac and Weyl fermions, but there are two different oscillation frequencies in the Zitterbewegung oscillations of Maxwell fermions [52]. Another idea is to generalize our 2D model in the presence of the time-reversal symmetry to test if the quantum spin Hall effect of the 2D Maxwell fermions

may occur. In that case, one can use the cold-atom system to simulate the quantum spin Hall effect of light [53], which has not yet been realized in experiments. Furthermore, the realization of Maxwell fermions will open the possibility to many applications, such as observing the above exotic topological fermions beyond Dirac and Weyl fermions, simulating the quantum behaviors of photons in matter, and simulating phenomena and solving problems related to quantum field theory. Therefore, our Maxwell fermions can shed new light on the understanding of Maxwell equations in quantum field theory and the topological excitations in condensed-matter physics or artificial systems.

In summary, we have systematically explored the topological Maxwell quasiparticles emerged in Maxwell metals and Maxwell insulators. The proposed models can be realized in optical lattices and the predicted exotic properties of these topological quasiparticles can be detected in cold-atom experiments.

APPENDIX A: REALIZATION OF 2D MAXWELL POINTS IN AN OPTICAL LIEB LATTICE

In this part, we show that the 2D Maxwell points and the associated Maxwell quasiparticles may be alternatively realized by using single-component fermionic atoms in optical lattices with three sublattices, such as an optical Lieb lattice [54]. In experiments, the optical Lieb lattice for cold atoms has been constructed by superimposing three types of optical lattices, with the tunable optical potential [54]

$$V(x,y) = -V_{\text{long}}^x \cos^2(k_L x) - V_{\text{long}}^y \cos^2(k_L y)$$
$$- V_{\text{short}}^x \cos^2(2k_L x) - V_{\text{short}}^y \cos^2(2k_L y)$$
$$- V_{\text{diag}} \cos^2\left[2k_L(x-y) + \frac{\pi}{2}\right]. \quad (A1)$$

Here $k_L = 2\pi/\lambda$ is a wave number of a long lattice with a depth V_{long}, a short lattice V_{short} is formed by laser beams at wavelength $\lambda/2$, and a diagonal lattice V_{diag} with the wave number $\sqrt{2}k_L$ is realized by interference of the mutually orthogonal laser beams at λ along the x and y directions. The optical Lieb lattice system is shown in Fig. 10(a), with three sublattices A, B, C forming a unit cell. By tuning the lattice depths $\{V_{\text{long}}, V_{\text{short}}, V_{\text{diag}}\}$, one can change the energy of the sublattices [54].

In this system, the pseudospin-1 basis is replaced by the three sublattices in a unit cell, and thus the three spin states are given by $|A\rangle \Leftrightarrow |\uparrow\rangle, |B\rangle \Leftrightarrow |0\rangle, |C\rangle \Leftrightarrow |\downarrow\rangle$. In this lattice, the spin-flip hopping $|B\rangle \leftrightarrow |C\rangle$ and $|A\rangle \leftrightarrow |C\rangle$ under the operators $\hat{S}_x$ and $\hat{S}_y$ along the x and y axis become naturally the nearest-neighbor hopping in that axis, with the corresponding hopping amplitudes shown in Fig. 10(a). With the similar Raman-assisted hopping method, the hopping along the x
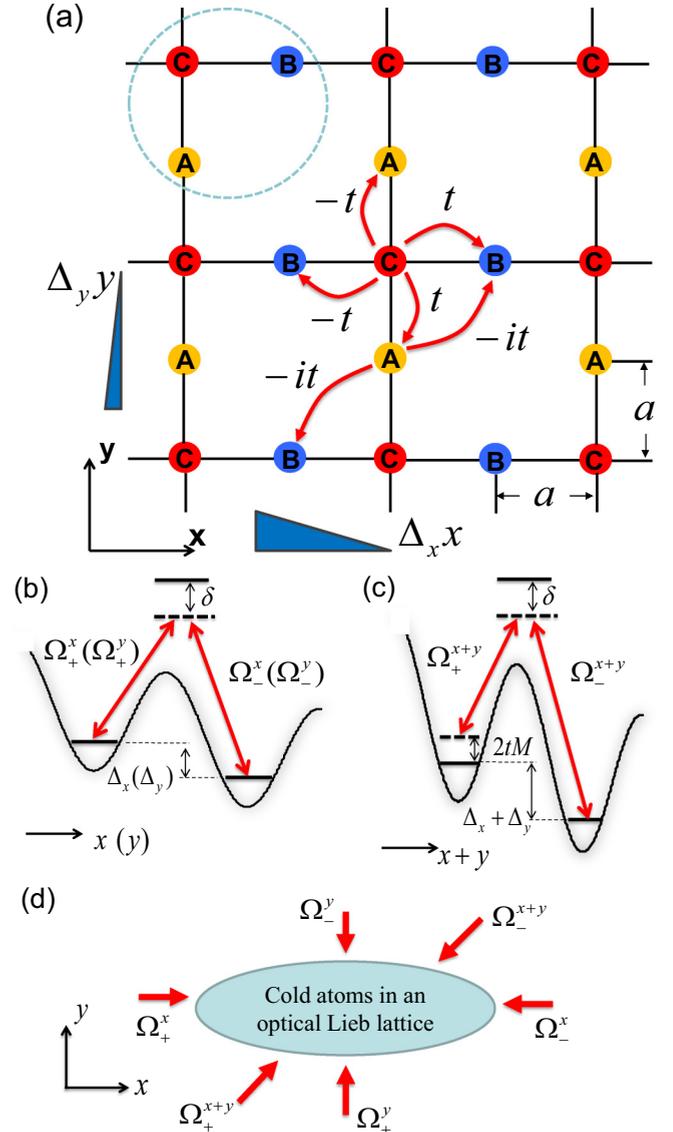

FIG. 10. (a) Schematic diagram of realizing 2D Maxwell fermions in an optical Lieb lattice. A unit cell indicated by dashed line is composed of three sites labeled by A, B, C, with the lattice constant a. The three sublattices form the pseudospin-1 basis, and the spin-flip hopping along each direction with the corresponding hopping amplitude is shown. This hopping can be realized by the Raman-assisted hopping method with the help of the linear title potentials $\Delta_x x$ and $\Delta_y y$ and the application of laser beams, similar to the scheme in the square optical lattice. (b) Two pairs of Raman beams for inducing the desired hopping along x and y directions; (c) a pair of Raman beams for inducing the desired hopping along $x + y$ direction and a two-photon detuning for inducing the constant term $2tM\hat{S}_z$; (d) the total lasers with the corresponding propagation direction.

axis and the y axis can be realized by two pairs of laser beams, $\Omega_{\pm}^x = \Omega_0 e^{\pm ik_1 x}$ and $\Omega_{\pm}^y = \pm\Omega_0 e^{\pm ik_1 y}$, under the large linear title potentials $\Delta_x x$ and $\Delta_y y$, respectively, as shown in Fig. 10(b). The detuning in each direction matches the frequency offset of the corresponding Raman beams as we can choose the title energies $\Delta_x \approx 2.5\Delta_y$ with $\Delta_y \gg t_0$ being

assumed. In this system, since only one atomic internal state is used in the Raman transitions, then one can address the atoms only through the energy selection without involving the laser polarization [32,33]. Under the two pairs of laser beams, the momenta transferred in the Raman transition along the x and y directions are $\delta\mathbf{k}_1 = -2k_1\hat{x}$ and $\delta\mathbf{k}_2 = -2k_2\hat{y}$, respectively. Thus the corresponding site-dependent hopping phases along x and y directions are $e^{-2ik_1 x} = e^{-2ik_1 j_x a}$ and $e^{-2ik_2 y} = e^{-2ik_2 j_y a}$, with the lattice site index (j_x, j_y). We can choose the parameters $k_1 = k_2 = \pi/2a$ to induce the hopping phases $e^{-i\pi j_x} = e^{-i\pi j_y} = 0, \pi$ staggered along the x and y directions, which lead to the desired hopping $|B\rangle \leftrightarrow |C\rangle$ and $|A\rangle \leftrightarrow |C\rangle$ in the corresponding axis.

The spin-flip hopping $|A\rangle \leftrightarrow |B\rangle$ under the operator $\hat{S}_z$ in this lattice becomes next-nearest-neighbor hopping along the $x + y$ or $x - y$ axis, with the corresponding hopping amplitude along the $x + y$ axis shown in Fig. 10(a). This hopping can be achieved by additional Raman transition by using the third pair lasers $\Omega_+^{x+y} = \Omega_0 e^{ik_3(x+y)}$ and $\Omega_-^{x+y} = -i\Omega_0 e^{-ik_3(x+y)}$ with a different matching energy $\Delta_x + \Delta_y = 3.5\Delta_y$, as shown in Fig. 10(c). Here a two-photon detuning in the transition can be used to induce the constant term $2tM\hat{S}_z$, without adding other coupling beams in this system. We choose the parameter $k_3 = \pi/a$, then the site-dependent phase along the $x + y$ direction can always be reduced to $e^{-2ik_3(j_x + j_y)a} = 1$, such that the hopping constant $-it$ along this direction is achieved by the two Raman beams. If the hopping $|A\rangle \leftrightarrow |B\rangle$ along the $x - y$ axis is wanted, one can also add the Raman transition with the matching energy $\Delta_x - \Delta_y = 1.5\Delta_y$. The laser configuration of this system is shown in Fig. 10(d). Under these conditions, the Bloch Hamiltonian of the 2D Maxwell systems now becomes

$$\mathcal{H}(\mathbf{k}) = R_x(\mathbf{k})\hat{S}_x + R_y(\mathbf{k})\hat{S}_y + R_z(\mathbf{k})\hat{S}_z,$$
$$R_x = 2t \sin k_x,$$
$$R_y = 2t \sin k_y,$$
$$R_z = 2t[M - \cos(k_x + k_y)]. \tag{A2}$$

Here the spin-1 matrices $\hat{S}_{x,y,z}$ acts on the three sublattices and the lattice constant $a \equiv 1$. In this case, one can obtain the Maxwell points and the associated Maxwell quasiparticles, similar to the case discussed in the main text. For instance, when the parameter $M = 1$, there is a Maxwell point at $\mathbf{K} = (0,0)$ with the low-energy effective Hamiltonian $\mathcal{H}_{\text{eff}}(\mathbf{q}) \approx vq_x\hat{S}_x + vq_y\hat{S}_y$, where $v = 2t$ is the effective speed of light and $\mathbf{q} = \mathbf{k} - \mathbf{K}$.

APPENDIX B: DERIVATION OF THE TOPOLOGICAL INVARIANTS

As we know, the Berry curvature is given by $\mathbf{F} = \nabla \times \mathbf{A}$, where the Berry connection is given by $\mathbf{A} = -i\langle\psi|\nabla\psi\rangle$. For the Bloch Hamiltonian of the 2D model in the main text $\mathcal{H} = \mathbf{R}(\mathbf{k}) \cdot \mathbf{S}$, the Berry connection $\mathbf{A} = (A_x, A_y, 0)$ for the lowest band with the energy $E = -R$ is given by [27]

$$A_\mu = -\frac{R_3}{R(R^2 - R_3^2)}\left(R_2\frac{\partial R_1}{\partial k_\mu} - R_1\frac{\partial R_2}{\partial k_\mu}\right). \tag{B1}$$

The corresponding Berry curvature is $\mathbf{F} = (0,0,F_{xy})$ with F_{xy} being given by

$$F_{xy} = \frac{\partial A_y}{\partial k_x} - \frac{\partial A_x}{\partial k_y}$$
$$= -\frac{1}{R^3}\varepsilon_{abc}R_a\frac{\partial R_b}{\partial k_x}\frac{\partial R_c}{\partial k_y}$$
$$= -\frac{1}{R^3}\mathbf{R} \cdot \left(\frac{\partial\mathbf{R}}{\partial k_x} \times \frac{\partial\mathbf{R}}{\partial k_y}\right), \tag{B2}$$

where the Bloch vectors are $R_x = 2t \sin k_x$, $R_y = 2t \sin k_y$, and $R_z = 2t(M - \cos k_x - \cos k_y)$. A straightforward calculation gives the following form:

$$F_{xy} = \frac{\cos k_x + \cos k_y - M \cos k_x \cos k_y}{[\sin^2 k_x + \sin^2 k_y + (M - \cos k_x - \cos k_y)^2]^{3/2}}. \tag{B3}$$

We can thus obtain the Chern number for this band

$$\mathcal{C} = \frac{1}{2\pi}\oint_S d\mathbf{k} \cdot \mathbf{F}(\mathbf{k})$$
$$= \frac{1}{2\pi}\oint_S d^2k\, F_{xy}$$
$$= \begin{cases} 2\,\text{sgn}(M), & (0 < |M| < 2), \\ 0, & (|M| > 2)h. \end{cases} \tag{B4}$$

For $M = \pm 2$, we respectively expand the Hamiltonian around $\mathbf{K}_+ = (0,0)$ and $\mathbf{K}_- = (\pi,\pi)$, and obtain the low-energy effective Hamiltonian

$$H_\pm(\mathbf{q}) = \pm(vq_x\hat{S}_x + vq_y\hat{S}_y - 2tm\hat{S}_z), \tag{B5}$$

where $m = 2 \mp M$, $v = 2t$, and $\mathbf{q} = \mathbf{k} - \mathbf{K}_\pm$ with $|\mathbf{q}| \ll |\mathbf{k}|$. We can obtain the effective Berry curvature

$$F_{xy} = \pm\frac{m}{(q^2 + m^2)^{3/2}}, \tag{B6}$$

where $q = \sqrt{q_x^2 + q_y^2}$. Thus the Berry phase γ integrated around the Maxwell point $\mathbf{K}_\pm$ for the Fermi surface can be derived by

$$\gamma = \oint_{FS} d\mathbf{k} \cdot \mathbf{A}(\mathbf{k}) = \pm\oint_{FS} d^2q\,\frac{m}{(q^2 + m^2)^{3/2}}$$
$$= \pm\int_0^{2\pi} d\theta\int_0^{k_F}\frac{m}{(q^2 + m^2)^{3/2}}q\,dq$$
$$= \pm2\pi\int_0^{k_F}\frac{m}{(q^2 + m^2)^{3/2}}q\,dq, \tag{B7}$$

where k_F is the Fermi momentum and the parameter $m \to 0$. Let $q = m\tan\varphi$; then we have $1 + \tan^2\varphi = \sec^2\varphi$ and $dq = m\sec^2\varphi\,d\varphi$. Substituting these relationships into the above equation, we obtain γ as a function of m:

$$\gamma = \pm2\pi\int_0^{k_F}\frac{m}{(q^2 + m^2)^{3/2}}q\,dq$$
$$= \pm2\pi\int_0^{\varphi_F}\frac{m^2\tan\varphi}{m^3\sec^3\varphi}m\sec^2\varphi\,d\varphi$$

$$= \pm 2\pi \int_0^{\varphi_F} \sin\varphi \, d\varphi$$

$$= \pm 2\pi \left(1 - \frac{m}{\sqrt{k_F^2 + m^2}}\right). \tag{B8}$$

Thus, for $m = 0$, we obtain $\gamma = \pm 2\pi$ for $M = \pm 2$.

For $M = 0$, we respectively expand the Hamiltonian around $\mathbf{K}_{(0,\pi)} = (0,\pi)$ and $\mathbf{K}_{(\pi,0)} = (\pi,0)$, and obtain the low-energy effective Hamiltonian

$$\mathcal{H}_0(\mathbf{q}) = \pm(vq_x \hat{S}_x - vq_y \hat{S}_y + 2tm_0 \hat{S}_z), \tag{B9}$$

where $m_0 = \pm M$ in this case, and $\mathbf{q} = \mathbf{k} - \mathbf{K}_{(0,\pi)/(\pi,0)}$, $|\mathbf{q}| \ll |\mathbf{k}|$. We can obtain the Berry connection

$$A_x = \pm \frac{m_0 q_y}{q^2 \sqrt{q^2 + m_0^2}},$$

$$A_y = \pm \frac{m_0 q_x}{q^2 \sqrt{q^2 + m_0^2}}. \tag{B10}$$

Thus the Berry phase γ integrated around the Maxwell point $\mathbf{K}_{(0,\pi)/(\pi,0)}$ for Fermi surface can be derived as

$$\gamma = \oint_{FS} d\mathbf{k} \cdot \mathbf{A}(\mathbf{k}) = \int_0^{2\pi} k_F d\theta \, A_\theta$$

$$= \int_0^{2\pi} k_F d\theta \left(A_y \frac{q_x}{k_F} - A_x \frac{q_y}{k_F}\right)$$

$$= \pm \frac{m_0}{\sqrt{k_F^2 + m_0^2}} \int_0^{2\pi} (\cos^2\theta - \sin^2\theta) d\theta$$

$$= \pm \frac{m_0}{\sqrt{k_F^2 + m_0^2}} \int_0^{2\pi} d\theta \cos(2\theta)$$

$$= 0, \tag{B11}$$

where we have used the relationships $q_x = k_F \cos\theta$ and $q_y = k_F \sin\theta$.

Below we calculate the monopole charge of the 3D Maxwell points. For the effective Hamiltonian around the Maxwell point $\mathbf{M}_+ = (0,0,\frac{\pi}{2})$ in the main text, we use a more simplified form

$$H(\mathbf{q}) = q_x \hat{S}_x + q_y \hat{S}_y + q_z \hat{S}_z \tag{B12}$$

and then we obtain the three energies given by $\epsilon_\pm = \pm|\mathbf{q}|$, $\epsilon_0 = 0$. Going to polar coordinates $(q_x, q_y, q_z) = |\mathbf{q}|(\sin\theta \cos\varphi, \sin\theta \sin\varphi, \cos\theta)$, the corresponding eigenfunctions are

$$\psi_\pm = \frac{1}{\sqrt{2}} \begin{pmatrix} \pm i \, \sin\varphi - \cos\theta \, \cos\varphi \\ \mp i \, \cos\varphi - \cos\theta \, \sin\varphi \\ \sin\theta \end{pmatrix},$$

$$\psi_0 = \begin{pmatrix} \sin\theta \, \cos\varphi \\ \sin\theta \, \sin\varphi \\ \cos\theta \end{pmatrix}. \tag{B13}$$

The relationship for Berry curvature in different coordinates is

$$F^i = \epsilon_{ijk} F_{jk} = \epsilon_{ijk} F_{\theta\varphi} \frac{\partial(\theta,\varphi)}{\partial(R_j, R_k)},$$

$$F_{\theta\varphi} = \partial_\theta A_\varphi - \partial_\varphi A_\theta, \tag{B14}$$

where $A_\theta = i\langle \psi|\nabla_\theta|\psi\rangle$, and $A_\varphi = i\langle \psi|\nabla_\varphi|\psi\rangle$. To each of these eigenfunctions, the associated U(1) Berry curvature is given by

$$\mathbf{F}(\mathbf{k})_\pm = \nabla \times i\langle \psi_\pm|\nabla|\psi_\pm\rangle = \mp \frac{\mathbf{k}}{|\mathbf{k}|^3},$$

$$\mathbf{F}(\mathbf{k})_0 = \nabla \times i\langle \psi_0|\nabla|\psi_0\rangle = 0. \tag{B15}$$

The integral of $\mathbf{F}(\mathbf{k})_\pm$ over any surface enclosing the Maxwell point $\mathbf{M}_+$ is

$$\mathcal{C}_\pm = \frac{1}{2\pi} \oint_S d\mathbf{k} \cdot \mathbf{F}(\mathbf{k})_\pm = \mp 2. \tag{B16}$$

Therefore, the monopole charge of the Maxwell point $\mathbf{M}_+$ for the lowest band is $\mathcal{C} = +2$. The monopole charge of the other Maxwell point $\mathbf{M}_-$ for the lowest band is obtained as $\mathcal{C} = -2$. Fortunately, we can obtain the formula of Berry curvature $\mathbf{F}(\mathbf{k})$ for the lowest band by using (B1) and (B2), which are given by

$$F^x = \sin k_x \cos k_y \sin k_z / G(\mathbf{k}),$$

$$F^y = \cos k_x \sin k_y \sin k_z / G(\mathbf{k}),$$

$$F^z = (M\eta - \cos k_x - \cos k_y - \eta \cos k_z)/G(\mathbf{k}), \tag{B17}$$

where $\eta = \cos k_x \cos k_y$ and $G(\mathbf{k}) = [\sin^2 k_x + \sin^2 k_y + (M - \cos k_x - \cos k_y - \cos k_z)^2]^{\frac{3}{2}}$. Thus one can easily get the Berry curvature $\mathbf{F}(\mathbf{q})$ around the Maxwell points.

[1] F. Wilczek, Why are there analogies between condensed matter and particle theory?, Phys. Today **51**(1), 11 (1998).

[2] A. H. C. Neto, F. Guinea, N. M. R. Peres, K. S. Novoselov, and A. K. Geim, The electronic properties of graphene, Rev. Mod. Phys. **81**, 109 (2009).

[3] X. Wan, A. M. Turner, A. Vishwannath, and S. Y. Savrasov, Topological semimetal and Fermi-arc surface states in the electronic structure of pyrochlore iridates, Phys. Rev. B **83**, 205101 (2011).

[4] S.-M. Huang, S.-Y. Xu, I. Belopolski, C.-C. Lee, G. Chang, B. Wang, N. Alidoust, G. Bian, M. Neupane, C. Zhang, S. Jia, A. Bansil, H. Lin, and M. Z. Hasan, A Weyl Fermion semimetal with surface Fermi arcs in the transition metal monopnictide TaAs class, Nat. Commun. **6**, 7373 (2015).

[5] H. Weng, C. Fang, Z. Fang, A. Bernevig, and X. Dai, Weyl Semimetal Phase in Noncentrosymmetric Transition Metal Monophosphides, Phys. Rev. X **5**, 011029 (2015).

[6] S.-Y. Xu, I. Belopolski, N. Alidoust, M. Neupane, G. Bian, C. Zhang, R. Sankar, G. Chang, Z. Yuan, C. C. Lee, S.-M. Huang, H. Zheng, J. Ma, D. S. Sanchez, B. Wang, A. Bansil, F. Chou, P. P. Shibayev, H. Lin, S. Jia, and M. Z. Hasan, Discovery of a Weyl fermion semimetal and topological Fermi arcs, Science **349**, 613 (2015).

[7] B. Q. Lv, H. M. Weng, B. B. Fu, X.-P. Wang, H. Miao, J. Ma, P. Richard, X.-C. Huang, L.-X. Zhao, G.-F. Chen, Z. Fang, X. Dai, T. Qian, and H. Ding, Experimental Discovery of Weyl Semimetal TaAs, Phys. Rev. X **5**, 031013 (2015).

[8] S.-Y. Xu *et al.*, Discovery of a Weyl fermion state with Fermi arcs in niobium arsenide, Nat. Phys. **11**, 748 (2015).

[9] N. Xu *et al.*, Observation of Weyl nodes and Fermi arcs in tantalum phosphide, Nat. Commun. **7**, 11006 (2016).

[10] L. Lu, Z. Wang, D. Ye, L. Ran, L. Fu, J. D. Joannopoulos, and M. Soljačić, Experimental observation of Weyl points, Science **349**, 622 (2015).

[11] W.-J. Chen, M. Xiao, and C. T. Chan, Photonic crystals possessing multiple Weyl points and the experimental observation of robust surface states, Nat. Commun. **7**, 13038 (2016).

[12] M. Z. Hasan and C. L. Kane, Topological insulators, Rev. Mod. Phys. **82**, 3045 (2010).

[13] X. L. Qi and S. C. Zhang, Topological insulators and superconductors, Rev. Mod. Phys. **83**, 1057 (2011).

[14] B. Bradlyn, J. Cano, Z. Wang, M. G. Vergniory, C. Felser, R. J. Cava, and B. A. Bernevig, Beyond Dirac and Weyl fermions: Unconventional quasiparticles in conventional crystals, Science **353**, aaf5037 (2016).

[15] Z. Lan, N. Goldman, A. Bermudez, W. Lu, and P. Öhberg, Dirac-Weyl fermions with arbitrary spin in two-dimensional optical superlattices, Phys. Rev. B **84**, 165115 (2011).

[16] L. Liang and Y. Yu, Rarita-Schwinger-Weyl semimetal in $J_{\text{eff}} = 3/2$ electron systems, Phys. Rev. B **93**, 045113 (2016).

[17] B. Q. Lv, Z. L. Feng, Q.-N. Xu, X. Gao, J.-Z. Ma, L.-Y. Kong, P. Richard, Y.-B. Huang, V. N. Strocov, C. Fang, H.-M. Weng, Y.-G. Shi, T. Qian, and H. Ding, Observation of three-component fermions in the topological semimetal molybdenum phosphide, Nature (London) **546**, 627 (2017).

[18] S.-L. Zhu, B.-G. Wang, and L. M. Duan, Simulation and Detection of Dirac Fermions with Cold Atoms in an Optical Lattice, Phys. Rev. Lett. **98**, 260402 (2007).

[19] D.-W. Zhang, Z. D. Wang, and S.-L. Zhu, Relativistic quantum effects of Dirac particles simulated by ultracold atoms, Front. Phys. **7**, 31 (2012); F. Mei, D.-W. Zhang, and S.-L. Zhu, Graphene-like physics in optical lattices, Chin. Phys. B **22**, 116106 (2013).

[20] L. Tarruell, D. Greif, T. Uehlinger, G. Jotzu, and T. Esslinger, Creating, moving and merging Dirac points with a Fermi gas in a tunable honeycomb lattice, Nature (London) **483**, 302 (2012).

[21] L. Duca, T. Li, M. Reitter, I. Bloch, M. Schleier-Smith, and T. Schneider, An Aharonov-Bohm interferometer for determining Bloch band topology, Science **347**, 288 (2015).

[22] A. Bermudez, L. Mazza, M. Rizzi, N. Goldman, M. Lewenstein, and M. A. Martin-Delgado, Wilson Fermions and Axion Electrodynamics in Optical Lattices, Phys. Rev. Lett. **105**, 190404 (2010).

[23] T. Dubcek, C. J. Kennedy, L. Lu, W. Ketterle, M. Soljacic, and H. Buljan, Weyl Points in Three-Dimensional Optical Lattices: Synthetic Magnetic Monopoles in Momentum Space, Phys. Rev. Lett. **114**, 225301 (2015); D.-W. Zhang, R.-B. Liu, and S.-L. Zhu, Generalized Hofstadter model on a cubic optical lattice: From nodal bands to the three-dimensional quantum Hall effect, Phys. Rev. A **95**, 043619 (2017)

[24] D.-W. Zhang, S.-L. Zhu, and Z. D. Wang, Simulating and exploring Weyl semimetal physics with cold atoms in a two-dimensional optical lattice, Phys. Rev. A **92**, 013632 (2015);

Y. Xu and L.-M. Duan, Type-II Weyl points in three-dimensional cold-atom optical lattices, *ibid.* **94**, 053619 (2016); W.-Y. He, S. Zhang, and K. T. Law, Realization and detection of Weyl semimetals and the chiral anomaly in cold atomic systems, *ibid.* **94**, 013606 (2016).

[25] R. Oppenheimer, Note on light quanta and the electromagnetic field, Phys. Rev. **38**, 725 (1931).

[26] R. Good and T. Nelson, *Classical Theory of Electric and Magnetic Fields* (Academic Press, New York, 1971).

[27] Y. He, J. Moore, and C. M. Varma, Berry phase and anomalous Hall effect in a three-orbital tight-binding Hamiltonian, Phys. Rev. B **85**, 155106 (2012).

[28] D. Xiao, W. Yao, and Q. Niu, Valley-Contrasting Physics in Graphene: Magnetic Moment and Topological Transport, Phys. Rev. Lett. **99**, 236809 (2007).

[29] N. Nagaosa, J. Sinova, S. Onoda, A. H. MacDonald, and N. P. Ong, Anomalous Hall effect, Rev. Mod. Phys. **82**, 1539 (2010).

[30] C. Fang, M. J. Gilbert, X. Dai, and B. A. Bernevig, Multi-Weyl Topological Semimetals Stabilized by Point Group Symmetry, Phys. Rev. Lett. **108**, 266802 (2012).

[31] T. O. Wehling, A. M. Black-Schaffer, and A. V. Balatsky, Dirac materials, Adv. Phys. **63**, 1 (2014).

[32] J. Dalibard, F. Gerbier, G. Juzeliūnas, and P. Öhberg, Artificial gauge potentials for neutral atoms, Rev. Mod. Phys. **83**, 1523 (2011).

[33] V. Galitski and I. B. Spielman, Spin-orbit coupling in quantum gases, Nature (London) **494**, 49 (2013).

[34] D. Jaksch and P. Zoller, Creation of effective magnetic fields in optical lattices: The Hofstadter butterfly for cold neutral atoms, New J. Phys. **5**, 56 (2003).

[35] H. Miyake, G. A. Siviloglou, C. J. Kennedy, W. C. Burton, and W. Ketterle, Realizing the Harper Hamiltonian with Laser-Assisted Tunneling in Optical Lattices, Phys. Rev. Lett. **111**, 185302 (2013).

[36] M. Aidelsburger, M. Atala, M. Lohse, J. T. Barreiro, B. Paredes, and I. Bloch, Realization of the Hofstadter Hamiltonian with Ultracold Atoms in Optical Lattices, Phys. Rev. Lett. **111**, 185301 (2013).

[37] C. J. Kennedy, W. C. Burton, W. C. Chung, and W. Ketterle, Observation of Bose-Einstein condensation in a strong synthetic magnetic field, Nat. Phys. **11**, 859 (2015).

[38] S. T. Wang, D. L. Deng, and L. M. Duan, Probe of Three-Dimensional Chiral Topological Insulators in an Optical Lattice, Phys. Rev. Lett. **113**, 033002 (2014).

[39] D. J. Thouless, Quantization of particle transport, Phys. Rev. B **27**, 6083 (1983); Q. Niu, Towards a Quantum Pump of Electric Charges, Phys. Rev. Lett. **64**, 1812 (1990).

[40] R. D. King-Smith and D. Vanderbilt, Theory of polarization of crystalline solids, Phys. Rev. B **47**, 1651 (1993); S. Coh and D. Vanderbilt, Electric Polarization in a Chern Insulator, Phys. Rev. Lett. **102**, 107603 (2009).

[41] N. Marzari, A. Mostofi, J. R. Yates, I. Souza, and D. Vanderbilt, Maximally localized Wannier functions: Theory and applications, Rev. Mod. Phys. **84**, 1419 (2012).

[42] L. Wang, A. A. Soluyanov, and M. Troyer, Proposal for Direct Measurement of Topological Invariants in Optical Lattices, Phys. Rev. Lett. **110**, 166802 (2013); L. Wang, M. Troyer, and X. Dai, Topological Charge Pumping in a One-Dimensional Optical Lattice, *ibid.* **111**, 026802 (2013); D.-W. Zhang, F. Mei, Z.-Y. Xue, S.-L. Zhu, and Z. D. Wang, Simulation and measurement

of the fractional particle number in one-dimensional optical lattices, Phys. Rev. A **92**, 013612 (2015); F. Mei, J.-B. You, D.-W. Zhang, X. C. Yang, R. Fazio, S.-L. Zhu, and L. C. Kwek, Topological insulator and particle pumping in a one-dimensional shaken optical lattice, *ibid.* **90**, 063638 (2014).

[43] S. Nakajima, T. Tomita, S. Taie, T. Ichinose, H. Ozawa, L. Wang, M. Troyer, and Y. Takahashi, Topological Thouless pumping of ultracold fermions, Nat. Phys. **12**, 296 (2016).

[44] M. Lohse, C. Schweizer, O. Zilberberg, M. Aidelsburger, and I. Bloch, A Thouless quantum pump with ultracold bosonic atoms in an optical superlattice, Nat. Phys. **12**, 350 (2016).

[45] H.-I. Lu, M. Schemmer, L. M. Aycock, D. Genkina, S. Sugawa, and I. B. Spielman, Geometrical Pumping with a Bose-Einstein Condensate, Phys. Rev. Lett. **116**, 200402 (2016).

[46] N. Fläschner, B. S. Rem, M. Tarnowski, D. Vogel, D.-S. Lühmann, K. Sengstock, and C. Weitenberg, Experimental reconstruction of the Berry curvature in a Floquet Bloch band, Science **352**, 1091 (2016).

[47] T. Li, L. Duca, M. Reitter, F. Grusdt, E. Demler, M. Endres, M. Schleier-Smith, I. Bloch, and U. Schneider, Bloch state tomography using Wilson lines, Science **352**, 1094 (2016).

[48] M. Aidelsburger, M. Lohse, C. Schweizer, M. Atala, J. T. Barreiro, S. Nascimbène, N. R. Cooper, I. Bloch, and N. Goldman, Measuring the Chern number of Hofstadter bands with ultracold bosonic atoms, Nat. Phys. **11**, 162 (2015).

[49] J. Y. Vaishnav, and C. W. Clark, Observing Zitterbewegung with Ultracold Atoms, Phys. Rev. Lett. **100**, 153002 (2008); D.-W. Zhang, Z.-Y. Xue, H. Yan, Z. D. Wang, and S.-L. Zhu, Macroscopic Klein tunneling in spin-orbit-coupled Bose-Einstein condensates, Phys. Rev. A **85**, 013628 (2012).

[50] Z. Li, H.-Q. Wang, D.-W. Zhang, S.-L. Zhu, and D.-Y. Xing, Dynamics of Weyl quasiparticles in an optical lattice, Phys. Rev. A **94**, 043617 (2016).

[51] Y. Xu and L.-M. Duan, Unconventional quantum Hall effects in two-dimensional triple-point fermion systems, arXiv:1705.05780.

[52] X. Shen *et al.* (unpublished).

[53] K. Y. Bliokh, D. Smirnova, and F. Nori, Quantum spin Hall effect of light, Science **348**, 1448 (2015).

[54] S. Taie, H. Ozawa, T. Ichinose, T. Nishio, S. Nakajima, and Y. Takahashi, Coherent driving and freezing of bosonic matter wave in an optical Lieb lattice, Sci. Adv. **1**, e1500854 (2015).